ISSN 1063-7788, Physics of Atomic Nuclei, 2024, Vol. 87, No. 9, pp. 1257–1280. © Pleiades Publishing, Ltd., 2024.
Russian Text © The Author(s), 2024, published in Yadernaya Fizika i Inzhiniring, 2024, Vol. 15, No. 6, pp. 522–546.

Study of the Radiation Hardening Mechanisms of Heat-Resistant Oxide Dispersion Strengthened Steels in Accelerated Tests Using Ion Irradiation and Ultramicroscopic Analysis

S. V. Rogozhkin[a, b, *], **A. A. Khomich**[a, b], **A. A. Nikitin**[a, b], **A. A. Bogachev**[a, b], **A. V. Klauz**[a, b], **P. A. Fedin**[a], **K. E. Pryanishnikov**[a], **T. V. Kulevoy**[a], **A. A. Lukyanchuk**[a, b], **O. A. Raznitsyn**[a, b], **A. S. Shutov**[a, b], **N. A. Iskandarov**[a, b], **A. G. Zaluzhny**[a, b], **M. V. Leontyeva-Smirnova**[c], **and A. A. Nikitina**[c]

[a] *National Research Centre Kurchatov Institute, Moscow, 123182 Russia*
[b] *National Research Nuclear University MEPhI (Moscow Engineering Physics Institute), Moscow, 115409 Russia*
[c] *Bochvar Advanced Research Institute of Inorganic Materials, Moscow, 123098 Russia*
**e-mail: Sergey.Rogozhkin@itep.ru, SVRogozhkin@mephi.ru*

Received April 16, 2024; revised April 16, 2024; accepted April 30, 2024

Abstract—Nanoscale mechanisms of radiation hardening of oxide dispersion-strengthened (ODS) heat-resistant steels EP-450 ODS and EP-823 ODS have been investigated after irradiation with 5.6-MeV Fe^{2+} ions with varying doses of radiation damage up to 100 dpa and temperatures in the range 350–500°C. The microstructure of the original and irradiated materials has been studied by transmission electron microscopy (TEM) and atom probe tomography (APT). The strengthening of the radiation-modified layer of irradiated samples has been studied by the dynamic indentation method. Initial state analysis of the steels has showed that EP-450 ODS steel contains a larger amount of small oxide particles (up to 20 nm) compared to EP-823 ODS steel. In addition, the density of nanosized Y–Ti–Cr–O clusters in EP-450 ODS steel is $\sim 10^{23}$ m^{-3}, which is two orders of magnitude higher than that in EP-823 ODS steel. At low irradiation doses, EP823 ODS steel demonstrates a higher radiation hardening rate at low irradiation temperatures compared to EP-450 ODS steel, and the rate of embrittlement decreases with increasing temperature. This is largely due to the formation of nanosized radiation-induced Ni–Mn–Si clusters with a high density in EP-823 ODS steel under the impact of irradiation. Other radiation-induced changes such as the rearrangement of the system of oxides and Y–Ti–Cr–O clusters, the formation of clusters predominantly enriched in Cr, and the formation of dislocation loops have been detected. It has been found that the radiation hardening of EP-450 ODS steel increases with the irradiation dose. In general, both steels demonstrate similar hardening at high irradiation doses.

Keywords: oxide dispersion-strengthened (ODS) steels, clusters, oxides, radiation loops, atom probe tomography, transmission electron microscopy, nanoindentation, ion irradiation, nanostructure

DOI: 10.1134/S1063778824090308

INTRODUCTION

A key element in the development of advanced nuclear facilities is the core materials, which must withstand high radiation loads (up to 200 displacements per atom (dpa)) and operate in a wide temperature range (from ~350 to 700°C). Programs for the development of materials that meet these requirements imply a transition from austenitic steels, which are prone to radiation swelling, to heat-resistant ferritic-martensitic steels [1, 2]. A high level of heat resistance is provided by dispersion-hardened oxide (DHO) ferritic-martensitic steels owing to a significant number of uniformly distributed oxide inclusions. The use of DHO steels is planned in many fourth-generation reactor facilities: for example, as a material for fuel element cladding in fast neutron reactors or as a structural material for the first wall of future thermonuclear reactors [3–8]. It has already been demonstrated that DHO steels can withstand required temperatures and doses of radiation damage [9, 10]. The mechanical properties of DHO steels significantly depend on the characteristics of the nanostructure: the size and spatial distribution of dispersed inclusions. Nanosized oxide inclusions are structural objects that impede the movement of dislocations; they can also ensure the capture of radiation defects and gas impurities (primarily helium) formed during transmutations.

Quantitative analysis of oxide inclusions in DHO steels requires the use of several complementary methods of microscopic analysis. The main method for analyzing inclusions was transmission electron

Table 1. Chemical composition of the EP-823 DHO and EP-450 DHO steel (wt %), iron balance

	Cr	Si	W	Nb	Mo	V	Mn	Ni	Mg	C	Y	Ti	Cu	O
EP-823 DHO	10.44	1.57	0.8	0.35	0.8	0.29	0.65	0.63	—	0.16	0.5	0.2	—	0.27
EP-450 DHO	13.1	0.23	0.003	0.35	1.61	0.18	0.44	0.12	0.0067	0.13	0.35	0.25	0.0087	0.32

microscopy (TEM) [2, 11–13]. Superfine oxide inclusions and clusters are detected using small-angle neutron scattering (SANS) [14–16] and small-angle X-ray scattering (SAXS) [17–19]. The most effective method for detecting the smallest inclusions is atomic probe tomography (APT) [20, 21]. Thus, the chemical composition of the inclusions larger than 5 nm is determined quite well by the methods of energy-dispersive analysis available in modern TEM, and the composition of inclusions on the order of nanometers can be studied in detail only with the help of APT. The APT studies have shown that the composition of nanoclusters in DHO steels differs from the composition of stoichiometric oxides. DHO steels contain a high density of nanoclusters enriched not only in Y and O but also in other alloying elements Cr, V, Ti, ... (present in the alloy composition) [22, 23]. Thus, ODS Eurofer steel developed in Europe within the framework of the program [24, 25] on thermonuclear reactors contains Y_2O_3 oxides [11, 12, 26] and nanoclusters enriched in Y, O, Cr, V, and N [20–22]. It should be noted that ODS Eurofer contains about 0.2 wt % V, and this chemical element plays an important role in the nucleation of clusters in ODS Eurofer. Ti is considered to be the most effective chemical element for the formation of nanostructures in DHO steels [1, 23]. Clusters in DHO steels with Ti in their composition are enriched in Y, O, and Ti, and their bulk density is higher than the density of clusters in ODS Eurofer (without Ti in the composition) [19, 22]. Clusters are an important element of the nanostructure of DHO steels. Recently, it has been shown that, only by taking into account clusters, it is possible to correctly estimate the hardness of many DHO steels on the basis of microscopy data, including TEM, APT, and SANS analysis [27].

Since the enhanced performance properties of DHO steels significantly depend on oxide nano-inclusions (particles and clusters) uniformly distributed in the matrix, close attention is paid to the study of the stability of the nanostructure of DHO steels [9, 10, 28, 29]. The general mechanisms of the effect of irradiation on ferritic-martensitic steels, as well as on the nanostructure of DHO steels, are well known; however, a detailed understanding of the effect of irradiation on the behavior of DHO steels has not yet been achieved.

It has been shown that irradiation in steels at room temperature can lead to the dissolution of large (>10 nm) oxides and the nucleation of clusters enriched in Y, O and V or Ti and small (<5 nm) oxide inclusions [30]. Increasing the irradiation temperature to 300°C and higher results in stabilization of oxide inclusions in most cases (see review [10]). Recent studies of a number of DHO steels have shown that low-temperature irradiation can lead to dissolution of large (>10 nm) and nucleation of small (<3 nm) oxide inclusions in the steels containing large inclusions, while this effect is suppressed in the steels with fine inclusions [31, 32]. Note that radiation-induced effects in DHO steels can significantly depend on the initial nanostructure: the density and sizes of oxides and nanoclusters. At low oxide inclusion densities, effects close to those observed in traditional ferritic-martensitic steels can be expected. In addition, because of the restructuring of the steel nanostructure, irradiation can also lead to radiation-induced effects characteristic of traditional steels. This behavior is typical of industrially produced DHO steels, while in model DHO steels and alloys of the latest generation, the densities of objects are maximally increased (noticeably more than 10^{22} m^{-3}) with a decrease in the sizes of these inclusions to 5 nm and less. The noted features of the initial DHO nanostructure can significantly affect the behavior of DHO steels under irradiation.

In Russia, a number of DHO steels are being developed, which are considered as materials for cladding of fuel elements for fast neutron reactors. At present, a wide range of products from EP-450 DHO [2, 13] and EP-823 DHO [33, 34] has been mastered. The aim of this work is a systematic comprehensive study of radiation-induced changes in Russian DHO steels EP-450 DHO and EP-823 DHO in the field of low-temperature radiation embrittlement in a wide range of doses of radiation damage under ion irradiation.

1. MATERIALS AND METHODS

This work studies the effect of irradiation on two steels, EP-450 DHO and EP-823 DHO, developed at JSC VNIINM. The samples in the form of plates measuring 10 × 20 × 0.4 mm were studied. The composition of the steels under study is presented in Table 1. The final heat treatment included hardening from 1150°C (exposure for 30 min) and tempering at 740°C for 2 h.

Preparation of samples for analysis of the initial state and for irradiation was carried out in several stages. At the first stage, blanks in the form of disks with a diameter of 3 mm and a thickness of ~300 μm were cut from the original sample of the material using electrical discharge cutting. At the second stage, mechanical thinning of the material blanks was carried out using SiC paper with a sequential decrease in the grain size from 15 to 5 μm. The final polishing was performed using a suspension of colloidal silicon oxide with a grain size of 40 nm. Electrochemical polishing of the samples was performed to remove the material layer damaged during mechanical thinning. At the end of the sample preparation, the surface of the blanks was cleaned from the electrolyte residues using ethanol. As a result, samples in the form of disks with a diameter of 3 mm and a thickness of 210 ± 10 μm were prepared for the studies.

Before and after ion irradiation, the surface quality of the prepared samples was controlled by atomic force microscopy (AFM) using a MultiMode Nanoscope IIIa multifunctional scanning probe microscope. For the original and irradiated samples, the average surface roughness and the greatest surface profile height were determined, which were no more than 17 and 110 nm after preparation and no more than 14 and 120 nm after irradiation.

Steel samples were irradiated on a TIPr-1 linear accelerator (heavy-ion prototype) [35, 36] with a beam of Fe^{2+} ions with an energy of 5.6 MeV in a pulsed mode with a pulse duration of 450 μs and a repetition rate of up to 2 s. The samples were irradiated in a vacuum of $(1.5–6.0) \times 10^{-7}$ Torr at temperatures of 350, 400, 450, and 500°C (the deviation from the specified temperature was no more than 3°C [37]). The temperature range was chosen to cover the temperature range of low-temperature radiation embrittlement, which determines the lower limit of the temperature range for the operation of steels. It should be noted that a number of studies have shown that the shift in the temperature of ion irradiation of ferritic-martensitic steels to compensate for the flax effect, compared to reactor irradiation, is ~50–60°C [38, 39]. The achieved irradiation fluences were $(0.5, 1.0, 1.7) \times 10^{17}$ cm^{-2}, so as to achieve different doses of radiation damage up to 100 dpa.

To calculate the damage profiles and ion implantation in the steel samples, the SRIM 2008 software package [40] was used. Figure 1 shows the damage profiles and the number of implanted ions when pure iron was irradiated with 5.6 MeV Fe^{2+} ions to a fluence of 1.7×10^{17} cm^{-2}. The results of calculations show that the region of maximum defect concentration and ion implantation is located at a depth of ~1.4 and ~1.6 μm from the sample surface, respectively. For microscopic analysis, an area at a depth of ~1 μm, remote from the surface and from the implantation zone, was selected. For the maximum fluence, the proportion of implanted Fe^{2+} ions in the study area of the material did not exceed 0.5 at %. Thus, for fluences of $(0.5, 1.0, 1.7) \times 10^{17}$ cm^{-2}, the doses of radiation damage in the study area were 30, 60, and 100 dpa. In some cases, the study was carried out at a depth of 0.5 μm, where the dose of radiation damage is two times less than the dose at a depth of 1 μm.

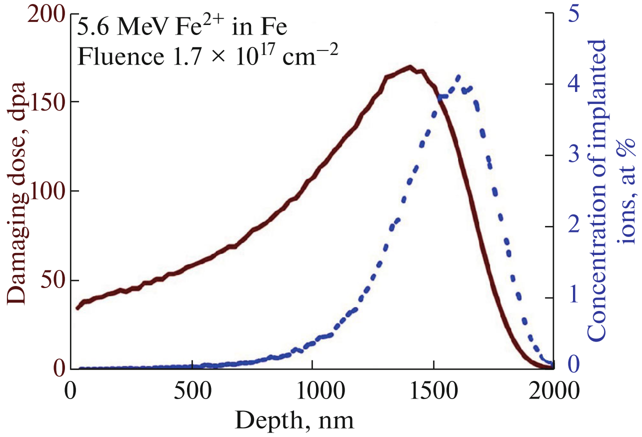

Fig. 1. Profile of radiation damage (solid line) and profile of ion implantation (dashed line) during irradiation of pure Fe with Fe^{2+} ions with energy of 5.6 MeV to fluence of 1.7×10^{17} cm^{-2}. Radiation damage was calculated in the Kinchin—Pease model with the energy of atomic displacement from crystal lattice sites of 40 eV.

The effect of irradiation on the structural-phase state of steels was studied using transmission electron microscopy (TEM) and atomic probe tomography (APT).

A HELIOS scanning electron-ion microscope was used to prepare samples for TEM in the form of cross sections from ion-irradiated steel samples. Samples for further microscopic studies were prepared using a focused beam of Ga^{+} ions at an accelerating voltage of 5 kV. In order to minimize the thickness of the amorphized layer formed during the interaction of the material with the Ga^{+} ion beam, the lamellae were polished at an accelerating voltage of 2 kV. The length of the cut TEM lamella of the material is ~4–5 μm. Thus, according to SRIM calculations, the size of the cut completely covers the region of maximum introduced damage and the region of ion stoppage in the material.

To study the microstructure of the samples, a Tecnai Osiris transmission electron microscope (FEI, United States) with a high-brightness electron source (X-FEG) and an accelerating voltage of 200 keV was used. The local chemical composition of the material was determined using a SuperX energy-dispersive X-ray spectrometer (FEI).

To study the initial state of the steels using atomic probe tomography methods, needle-shaped samples were prepared from the original plates. When analyzing the initial state of the materials, blanks measuring 0.3 × 0.3 × 15 mm were made by electrical discharge cutting in water. These blanks were then polished in bulk and a drop of a 2% solution of perchloric acid in dibutoxyethanol at a voltage of ~10 V. When studying

Table 2. Average size and bulk density of oxide particles in the initial state of EP-450 DHO and EP-823 DHO steels

Material	Average size of oxides, nm	Bulk density of oxides, 10^{21} m^{-3}
EP-450 DHO	10 ± 4	3.4 ± 0.7
EP-823 DHO	15 ± 5	2.4 ± 0.5

the irradiated materials, the samples for tomographic atomic probe studies were also prepared using a HELIOS NanoLab 600 scanning electron microscope. The studied volume of material was extracted from a depth of ~1 μm from the irradiated surface. The extracted volume was attached to a massive base and then polished with 30 keV Ga ions to a needle shape. The final polishing of the tip to the required dimensions (≤100 nm in diameter) was performed with Ga ions with energy of 2 keV. The final shape of the samples was controlled in a JEOL 1200 EX transmission electron microscope.

A PAZL-3D atomic probe tomograph with laser evaporation was used for the study using the APT methods [41]. The conditions of the study were as follows: the temperature of the sample was 50 K, the voltage on the sample was 2–10 kV, the laser wavelength was 355 nm, the laser pulse frequency was 100 kHz, the evaporation rate was from 2 to 25 atoms per 1000 laser impacts, the laser power was selected so that the ratio of singly and doubly charged ions was in the range from 100 to 500 relative units, and the pressure in the analysis chamber was no higher than 1×10^{-9} Torr. Atomic probe data were processed using the KVANTM-3D software [42]. The algorithm for reconstructing 3D atomic maps is based on a common algorithm for determining the radius of curvature of the tip of the sample on the basis of the stress on the sample [43] and selecting the image compression factor (ICF) [44]. The mass spectrum was reconstructed and optimized according to the protocol [45].

The strength characteristics of the steel samples in the initial state and after ion irradiation were analyzed using a NanoScan-4D scanning nanohardness tester with a Berkovich-type diamond triangular pyramid indenter. The indentation diagram was recorded and the hardness and elastic modulus were then calculated according to GOST 8.748-2011 (ISO 14577). The measurements were performed in the dynamic indentation mode [46] with the following indenter parameters: immersion depth of 2.5 μm; loading time of 60 s; oscillation frequency of 10 Hz; oscillation amplitude of 20 nm.

In order to eliminate the "indenter size effect," which is expressed as a nonlinear dependence of the hardness H on the indentation depth h, the model of "geometrically necessary dislocations" proposed by Nix and Gao in [47] was used. On the Nix–Gao diagram, the hardness of the irradiated layer of the sample was determined as a result of a linear approximation of the points of the H^2 versus $1/h$ graph in the range from 4.3 to 10.0 μm^{-1}, which corresponds to an indenter depth from 100 to 240 nm. To determine the correspondence between the indentation depth and the actual thickness of the sample layer, the following rule was used: the indentation depth corresponds to the layer thickness that exceeds the indenter immersion depth by six times [48].

Atomic force microscopy (AFM) was used to account for the plastic ridges that arise along the edges of the indentations. The appearance of plastic ridges leads to an underestimation of the contact area compared to the actual one and, as a result, to biased estimates of the material hardness. At least four indentations were scanned on each sample using AFM to determine the ratio of the hardness obtained using the nanohardness tester to the real hardness (calculated as the ratio of the load to the indentation area). The calculation was carried out using the formula proposed in [49]:

$$H_{\text{o-p}}/H = (1 + h_{\text{p-up}}/h_r)^2, \quad (1)$$

where $H_{\text{o-p}}$ is the hardness measured during instrumental indentation, $h_{\text{p-up}}$ is the indentation height, h_{r} is the residual indentation depth, and H is true hardness of the material.

The coefficients obtained in this way for each series of measurements were used to correct the hardness values of the irradiated layer of the samples under study.

2. RESULTS OF TEM STUDIES

The TEM studies, including scanning transmission electron microscopy (STEM), showed that EP-450 DHO steel mainly consists of sorbite grains elongated in one direction with characteristic sizes from 0.3 μm to 10 μm. An insignificant proportion of rounded delta-ferrite grains with sizes in the range from 0.5 μm to 8 μm was also found.

Oxide particles are observed inside the grains of EP-823 DHO and EP-450 DHO steels, partially coherent with the matrix and having a weak contrast in TEM images, obtained in the bright field mode. Typical HAADF images of oxide particles in the studied materials are shown in Figs. 2a and 3a. The results of the quantitative analysis of the observed oxide particles in the initial state of the studied DHO steels are presented in Table 2.

Second-phase precipitates ~10–20 nm in size are mainly oxides of the $Y_2Ti_2O_7$ type, which are semicoherent with the ferrite matrix of steel. They also contain oxide particles of the Y_2TiO_5 type and others. Note that, in the region of small sizes (less than 10 nm), it is quite difficult to establish stoichiometry. In addition, the steels under study contain large oxide particles larger than 60 nm, as well as carbides of the MC or

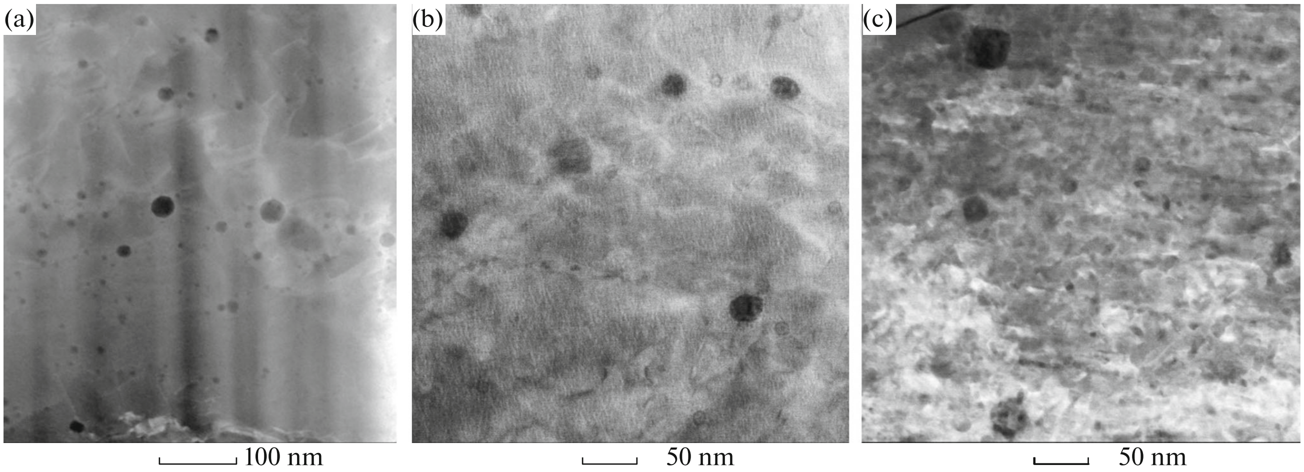

Fig. 2. Typical HAADF image of oxide particles in the EP-450 DHO steel: (a) in the initial state and irradiated to a dose of 60 dpa; (b) at 350°C; (c) at 500°C.

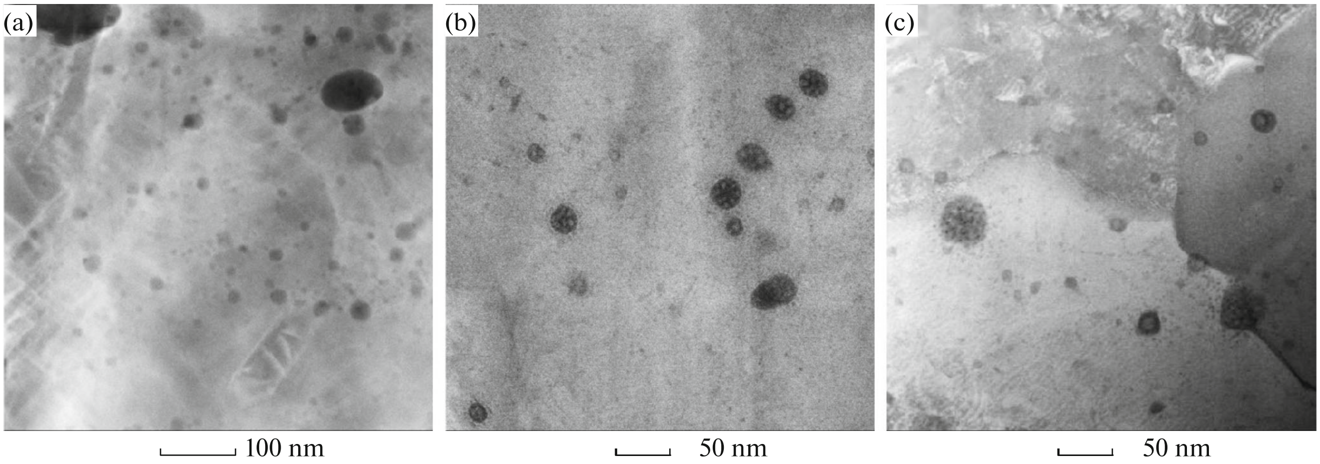

Fig. 3. Typical HAADF image of oxide particles in the EP-823 DHO steel: (a) in the initial state and irradiated to a dose of 60 dpa; (b) at 350°C; (c) at 500°C.

$M_{23}C_6$ type. The bulk density of large oxides is ~10^{19} m^{-3}, which is two orders of magnitude less than the bulk density of small oxides. In this regard, only oxides smaller than 60 nm in size were taken into account in the quantitative analysis, and the contribution of larger objects to the obtained oxide characteristics was estimated as insignificant.

The key difference between the studied samples of the materials studied in this work is the spatial distribution of small oxides: EP-450 DHO steel is strengthened by oxide particles of smaller size and with a higher bulk density than oxides in EP-823 DHO steel.

In the microstructure of EP-450 DHO steel irradiated with Fe ions to a dose of 30, 60 and 100 dpa at 450 and 500°C, the formation of nanosized pre-precipitations is observed (Fig. 2c). Low contrast relative to the matrix and small sizes (<5 nm) of pre-precipitations complicate their quantitative analysis by TEM methods. However, the bulk density of the observed clusters increases with increasing irradiation temperature. Presumably, there is a decomposition of the chromium matrix of EP-450 DHO steel after ion irradiation at high temperatures.

In the presented images of EP-823 DHO steel irradiated with ions, contrasting light areas in the form of individual dots are observed inside large oxide particles (>10 nm) (Figs. 3b and 3c). In addition, the formation of nanosized objects with high density around large oxides was detected. Because of the extremely small size (<3 nm) of these objects, their quantitative analysis by transmission electron microscopy is impossible. The observed effect can be explained by the redistribution of chemicals between the oxides and the matrix of the material as a result of radiation-

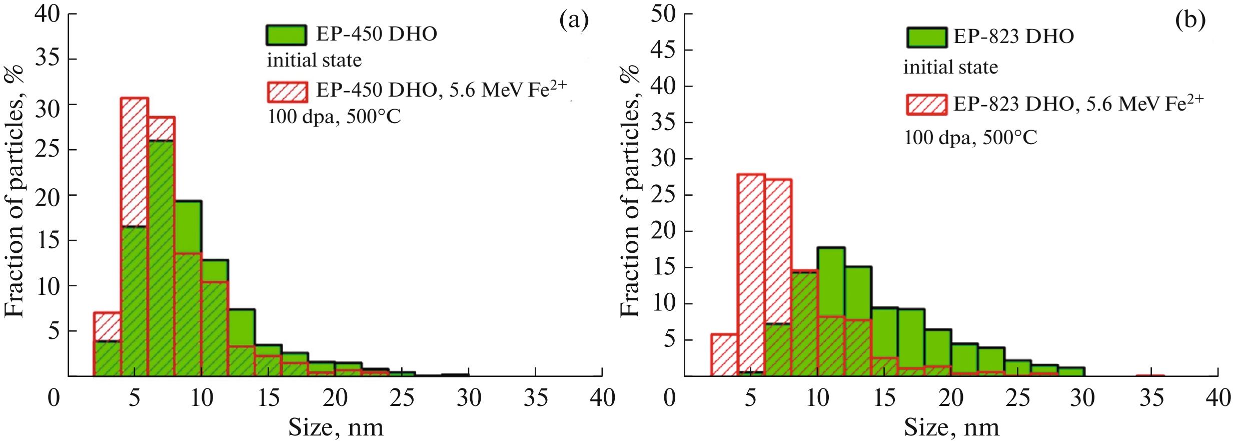

Fig. 4. Histograms of size distribution of oxide particle in steel: (a) EP-450 DHO, (b) EP-823 DHO in the initial state and after irradiation with 5.6 MeV Fe^{2+} ions at 500°C to a dose of 100 dpa.

induced breakdown of oxide particles under irradiation. At a dose of 60 dpa, the breakdown of particles is more pronounced than at 30 dpa, but the dependence of the effect on the irradiation temperature is not observed.

Quantitative analysis of the observed oxide inclusions in the studied materials showed that, in EP-450 DHO steel irradiated at 500°C, an increase in the proportion of oxides smaller than 10 nm is observed by ~5% and ~15% for the doses of 60 and 100 dpa (Fig. 4a), respectively. In the EP-450 DHO steel samples irradiated to 60 and 100 dpa at 350°C and 400°C, a shift in the oxide size distributions toward large oxides (larger than 10 nm in size) was detected. A slight increase in the proportion of large oxides occurs after irradiating EP-450 DHO to 60 dpa at 450°C.

In the EP-823 DHO steel, after irradiation to doses of 60 and 100 dpa, dissolution of large oxide inclusions (larger than 10 nm in size) was detected with the formation of a new fraction of small oxides (less than 10 nm). An increase in the irradiation temperature leads to an increase in the observed effect and an increase in the proportion of oxides smaller than 10 nm in size by ~55% at 500°C (Fig. 4b).

Figures 5 and 6 show the graphs of the dependence of the bulk density and average size of oxides on the irradiation temperature in the studied DHO steels irradiated to doses of 30, 60, and 100 dpa. In the EP-823 DHO steel samples irradiated to a dose of 30 dpa, the average sizes of oxides and their bulk density remain virtually unchanged compared to the initial state at all irradiation temperatures of 350–500°C. With an increase in the irradiation dose to 60 and then to 100 dpa, a clear tendency towards a decrease in the average sizes of oxides is visible. The bulk density of oxides increases with an increase in the dose from 30 to 60 dpa, but for temperatures of 400 and 450°C, no changes are found in the dose range of 60–100 dpa, and at 500°C, there is a decrease in the density of oxides upon the transition from 60 to 100 dpa. The highest bulk density of oxide inclusions is observed at an irradiation temperature of 400°C and for a dose of 100 dpa and is $(5 \pm 1) \times 10^{21}$ m^{-3} with an average oxide size of (8 ± 3) nm.

Oxide particles in EP-450 DHO steel are relatively more stable under irradiation. Some decrease in the average oxide size and increase in density with an increase in the irradiation dose of EP-450 DHO steel is observed only for 450 and 500°C.

Thus, smaller oxides (on average 10 nm) in the EP-450 DHO steel are quite stable: at temperatures of at least 400°C, they first grow and then gradually decrease. In this case, their growth is accompanied by a slight decrease in the density, and then with a decrease in the size, the density increases. Larger oxides (on average 15 nm) in EP-823 steel decrease with an increase in the irradiation dose, and their density increases with the dose.

In addition to the radiation-induced rearrangement of the nanostructure of the ferritic-martensitic steels, the formation of dislocation loops, a characteristic radiation defect in ferritic-martensitic steels, was detected under irradiation. Figures 7 and 8 show typical STEM images of the studied steel samples irradiated to a dose of 60 dpa at 350°C and 500°C. The figures also show deciphered diffraction patterns that determine the current orientation of the studied grain relative to the zone axis. The sets of images were obtained from the grains oriented along the zone axis of the $\langle 100\rangle$ and $\langle 110\rangle$ types.

The detected loops were of the $a\langle 100\rangle$ type. The number of registered loops of the $1/2a\langle 111\rangle$ type was negligibly small. The thickness of the TEM lamellae was measured using the characteristic electron energy loss spectroscopy (EELS) method. The quantitative analysis of the observed radiation-induced structural defects and the dependence of the bulk density and the

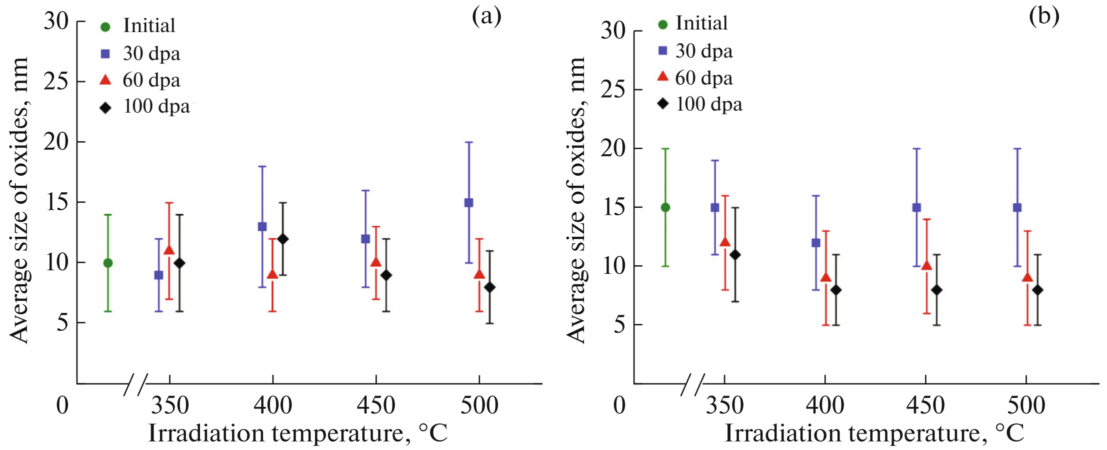

Fig. 5. Dependence of the average size of oxide particles on the irradiation temperature at damaging doses of 30, 60, and 100 dpa in steels: (a) EP-450 DHO and (b) EP-823 DHO.

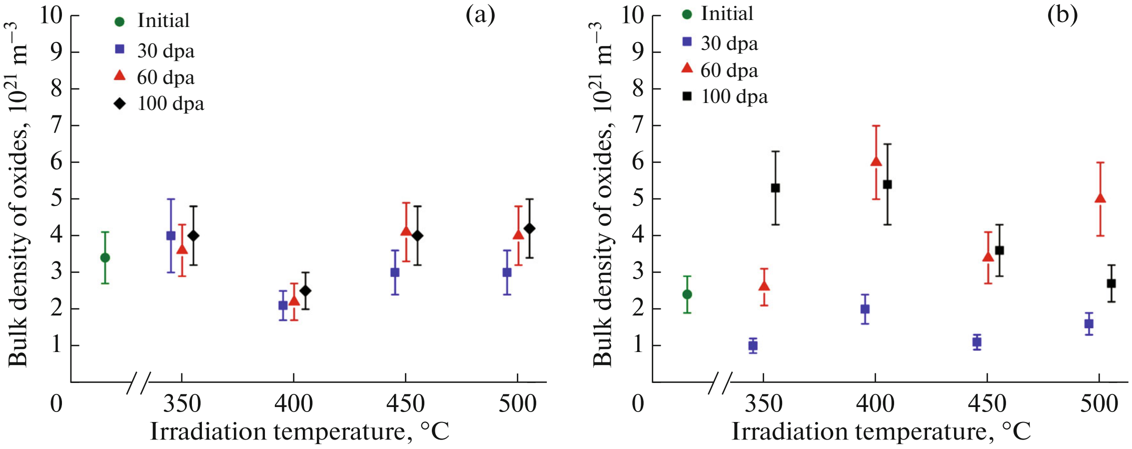

Fig. 6. Dependence of the bulk density of oxide particles on the irradiation temperature at damaging doses of 30, 60, and 100 dpa in steels: (a) EP-450 DHO and (b) EP-823 DHO.

average size of dislocation loops on the irradiation temperature in all the studied states are shown in Figs. 9 and 10.

The most obvious dependences for both EP-450 DHO and EP-823 DHO steels are observed with an increase in the irradiation temperature from 350 to 500°C: the average size of dislocation loops increases, and the density decreases. When irradiated to 100 dpa at a temperature of 500°C, the average loop size in EP-450 DHO steel is 12 ± 4 nm, and in EP-823 DHO steel, it is 14 ± 6 nm. It is quite difficult to note obvious dose dependences, although in most cases, at a maximum irradiation dose of 100 dpa, the loop size is slightly higher, and the density is lower compared to a dose of 30 dpa.

Local chemical analysis of the studied samples after irradiation to a maximum fluence of 1.7 × 10^{17} cm^{-2} was performed using X-ray energy-dispersive spectroscopy methods. Bright-field STEM images of the EP-450 DHO and EP-823 DHO steels taken in the HAADF mode at a depth of 0.5 μm (where the irradiation dose was 60 dpa), as well as the maps of chemical elements corresponding to the selected areas, are shown in Figs. 11 and 12. In the studied DHO steels irradiated with ions at 400, 450 and 500°C, the formation of pre-precipitations enriched in Cr is observed. The most intense decomposition regarding chromium is observed at 450°C. In addition, areas enriched in Ni were found in the steels. The highest density of pre-precipitations enriched in Ni is observed in the samples irradiated at 450°C. In all the studied samples, particles enriched in Y, Ti, and O were found, as well as particles enriched in Al (presumably Al_2O_3). In the EP-450 DHO steel, particles enriched in Nb and Ti are present (Fig. 13).

For a more accurate assessment of radiation-induced changes in the local chemical composition

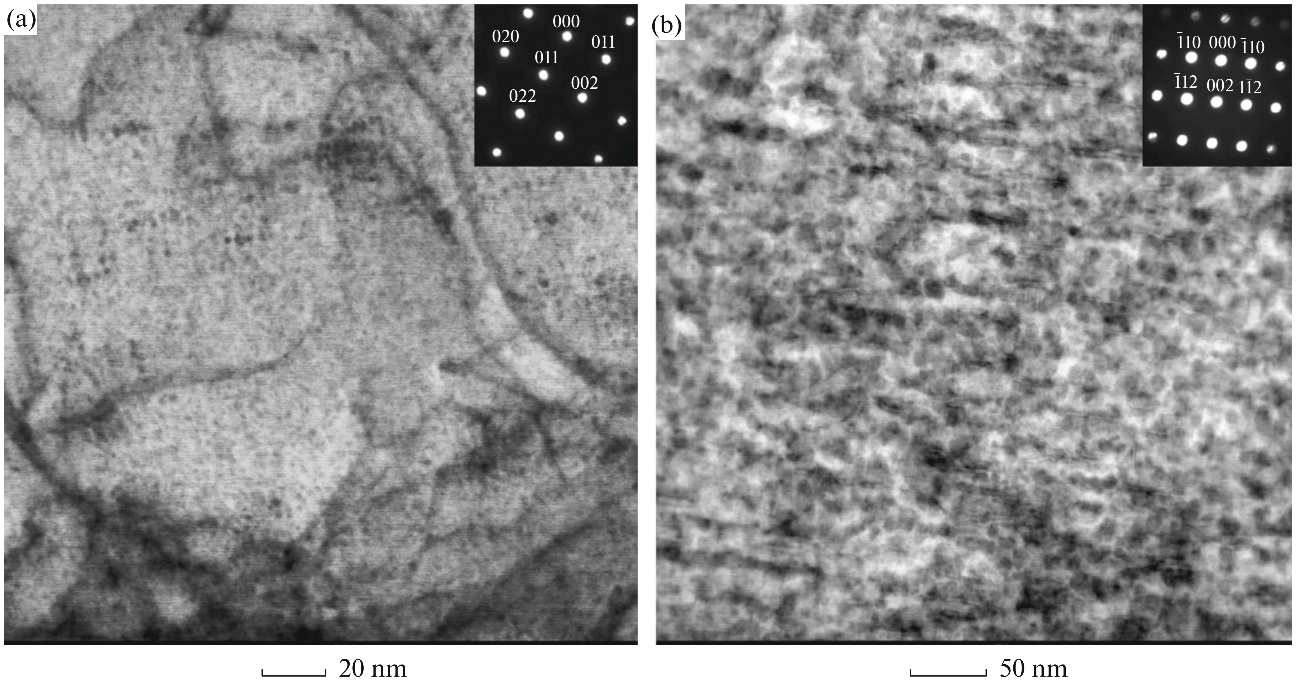

Fig. 7. Bright-field STEM images of dislocation loops in the EP-450 DHO steel irradiated with 5.6 MeV Fe^{2+} ions to a dose of 60 dpa at a temperature of (a) 350°C and (b) 500°C. The diffraction patterns from the studied grains with the orientation to the incident beam are shown: (a) [100] and (b) [110].

and nanostructure of the materials, an APT study was further carried out.

3. RESULTS OF RESEARCH BY APT METHODS

3.1. Atomic Distributions in the Initial State of DHO Steels

In EP-450 DHO steel, the APT method revealed a noticeable number of nanosized clusters and matrix regions enriched in a number of chemical elements; in addition, they are difficult to resolve by TEM methods, unlike oxide particles of the same size, since they do not have their own crystal lattice. Clusters of EP450 DHO steel are predominantly enriched in Cr, Ti, Y, and O and to a lesser extent in Mo, Ni, Mn, and V (hereinafter, we will call such formations Y–Ti–Cr–O clusters). Unlike oxides, which contain mainly Y, Ti and O, clusters contain these elements in smaller quantities and are also enriched in Cr and V. The average cluster size is (4 ± 1) nm, and the bulk density is ~3×10^{23} m^{-3}. Figure 14 shows the atomic maps of one of the studied bulks. The average content of chemical elements in the bulk and clusters, as well as in the matrix surrounding the clusters, is presented in Table 3.

Table 3. Concentrations of chemical elements in the matrix, in the studied volume, and in clusters for EP-450 DHO steel in the initial state, at %

Element	Matrix	Clusters
Cr	15.3 ± 0.3	18 ± 1
Si	0.45 ± 0.06	0.23 ± 0.1
Mn	0.47 ± 0.06	0.6 ± 0.2
V	0.32 ± 0.05	1.0 ± 0.2
C	0.02 ± 0.01	0.03 ± 0.03
Fe	82.4 ± 0.3	44 ± 1
Ni	0.20 ± 0.04	—
Ti	0.04 ± 0.02	14.1 ± 0.9
Mo	0.76 ± 0.08	0.6 ± 0.2
O	0.09 ± 0.03	16.2 ± 0.9
Y	—	3.9 ± 0.5

Analysis of the three-dimensional distribution of atoms by atomic probe tomography methods of the initial state of EP-823 DHO steel did not reveal any peculiarities. Almost all studied bulks represent a homogeneous solution. Only in one of the studied bulks, a Y–Ti–Cr–O cluster ~5 nm in size (Fig. 15), enriched in Cr, O, Ti and Y (Table 4), was detected. This result is in good agreement with the STEM results, according to which the bulk density of small oxide inclusions is low and amounts to ~10^{21} m^{-3}. The probability of detecting such objects with such a low bulk density by the APT method is extremely low.

Thus, EP-450 DHO and EP-823 DHO steels have a fundamental difference on the nanoscale. In EP450

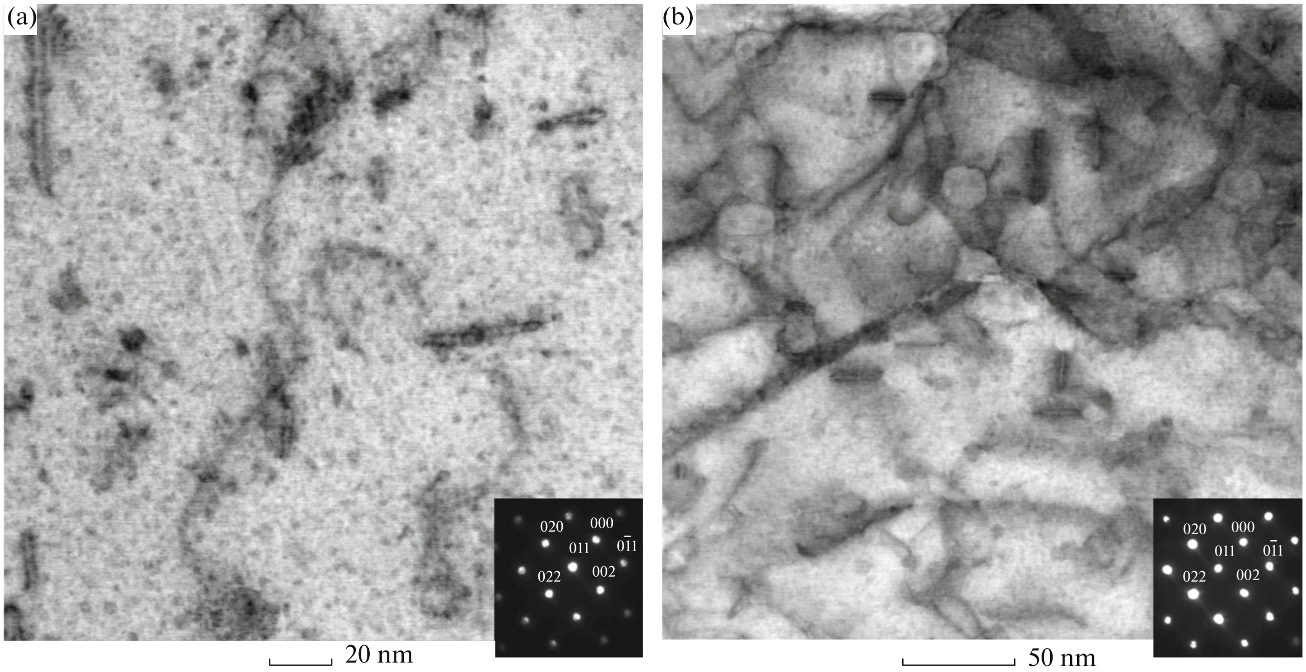

Fig. 8. Bright-field STEM images of dislocation loops in the EP-823 DHO steel irradiated with 5.6 MeV Fe^{2+} ions to a dose of 60 dpa at a temperature of (a) 350°C and (b) 500°C. The diffraction patterns from the studied grains with the orientation to the incident beam [100] are shown.

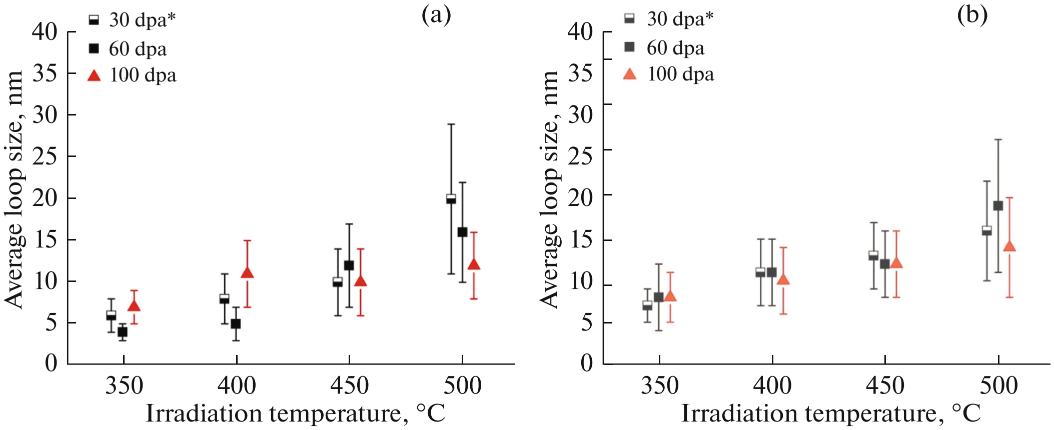

Fig. 9. Dependence of the average size of dislocation loops on the irradiation temperature at damaging doses of 30*, 60, and 100 dpa in steels: (a) EP-450 DHO and (b) EP-823 DHO. *The dose of 30 dpa is achieved at a depth of 0.5 μm in the steel samples irradiated to 60 dpa.

DHO steel, a significant number of Y—Ti—Cr—O clusters was found, which are typical of many DHO steels, while in EP-823 DHO steel, such clusters are practically absent.

3.2. Atomic Distributions in DHO Steels after Irradiation

The initial state of EP-450 DHO steel is characterized by the presence of a large number of oxide clusters of the Y—Ti—Cr—O type (~10^{23} m^{-3}). The APT studies after the irradiations showed that the nanostructure of EP-450 DHO steel is very stable, and a large number of Y—Ti—Cr—O clusters were also found in most of the studied irradiated states. An example of an atomic map of irradiated EP-450 DHO steel is shown in Fig. 16. The detected clusters have sizes from 2 to 5 nm and bulk density of ~10^{23} m^{-3} (Figs. 17 and 18).

It is evident from Figs. 17 and 18 that, with each step of increasing the irradiation dose, clusters (with a density of 10^{22}–10^{23} m^{-3}) are detected starting from a

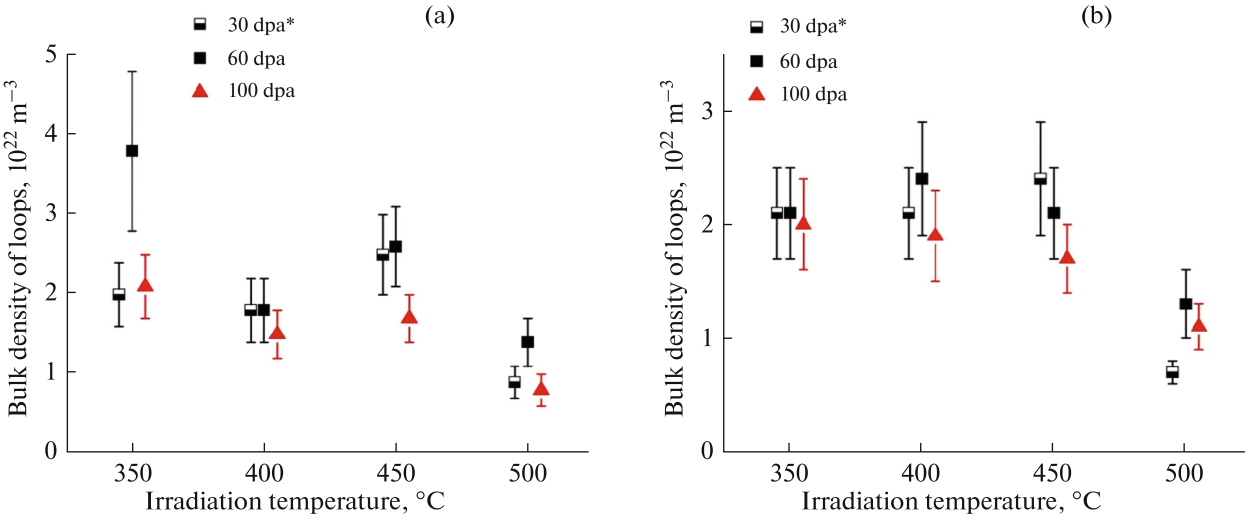

Fig. 10. Dependence of the bulk density of dislocation loops on the irradiation temperature at damaging doses of 30, 60, and 100 dpa in steels: (a) EP-450 DHO and (b) EP-823 DHO. *The dose of 30 dpa is achieved at a depth of 0.5 μm in the steel samples irradiated to 60 dpa.

higher temperature. Thus, at 30 dpa, clusters are detected at 350°C and higher temperatures; at 60 dpa, starting from 400°C; and at 100 dpa, starting only from 450°C.

After irradiation up to 30 dpa, with increasing temperature, a tendency towards a slight decrease in the average cluster size is observed, while the bulk density varies from temperature to temperature in a wide range of values from ~2 × 10^{23} to ~6 × 10^{23} m^{-3}. Such fluctuations in the bulk density can be associated with the locality of the method and the heterogeneity of the material itself from grain to grain. In addition, the STEM method showed that a large number of nanosized objects are formed around a large oxide particle under irradiation. The APT study zone that fell into such an area may lead to some distortions in the density assessment.

Table 4. Values of concentrations of elements in the studied volumes of solid solution of EP-823 DHO steel (content of chemical elements is given in at %)

	Matrix	Ti–O–Y cluster
Fe	83.5 ± 0.6	62 ± 1
Cr	11.3 ± 0.5	17.4 ± 0.8
Si	2.4 ± 0.2	1.7 ± 0.3
V	0.5 ± 0.1	2.5 ± 0.3
Mn	1.0 ± 0.2	1.4 ± 0.3
Mo	0.36 ± 0.09	0.3 ± 0.1
C	0.02 ± 0.02	0.6 ± 0.2
Ni	0.38 ± 0.09	1.2 ± 0.3
O	0.10 ± 0.05	4.9 ± 0.5
N	0.05 ± 0.03	1.3 ± 0.2
Cu	0.08 ± 0.04	0.4 ± 0.1
Co	0.01 ± 0.02	0.03 ± 0.03
W	0.18 ± 0.06	0.4 ± 0.1
Ti	0.09 ± 0.04	4.4 ± 0.5
Y	—	1.5 ± 0.3

After irradiation to a dose of 60 dpa and 100 dpa, the average cluster size remains stable within the error from temperature to temperature for both doses. The bulk density of clusters under irradiation to 60 dpa does not change with an increase in temperature from 400°C to 450°C (~3 × 10^{22} m^{-3}) and increases significantly at 500°C to ~10^{22} m^{-3}.

Figure 19 shows a histogram of cluster enrichment relative to the matrix. After irradiation to 30 dpa, no qualitative changes in the composition of Y–Ti–Cr–O clusters occur at different temperatures. Just as in the initial state, they are enriched in Cr, Ti, O, and Y to varying degrees. However, at 400°C, these clusters are depleted in Cr.

At 60 dpa, noticeable changes occur in the composition of Y–Ti–Cr–O clusters. At 400°C, enrichment in Y and O increases by several times, and insignificantly in Cr compared to the same temperature at 30 dpa. With increasing temperature, a tendency is observed for an increase in enrichment of clusters in Cr and for a decrease in enrichment in other elements.

The Y–Ti–Cr–O clusters found at temperatures of 450°C and 500°C after irradiation to 100 dpa differ in their chemical composition from the clusters found at lower doses. Enrichment in Cr corresponds to the level of the initial state, and the Y content is less than its content in the clusters of the initial state. The clusters consist mainly of Ti and O. Moreover, with an

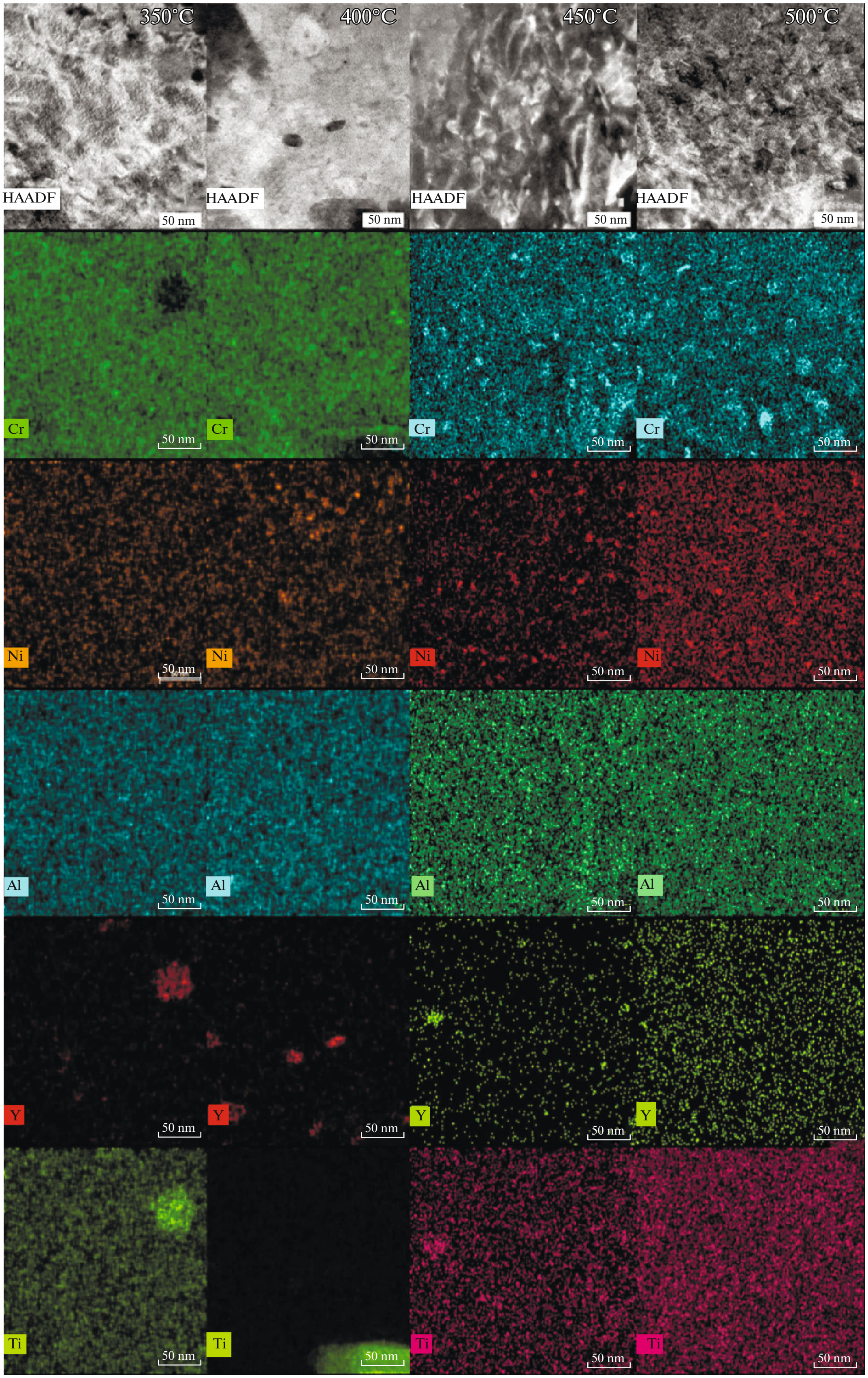

Fig. 11. Bright-field STEM images and corresponding EDX maps of chemical elements of the EP-823 DHO steel irradiated to 60 dpa at 350, 400, 450, and 500°C (fluence of 1.7×10^{17} cm^{-2}, study at a depth of 0.5 μm from the irradiated surface).

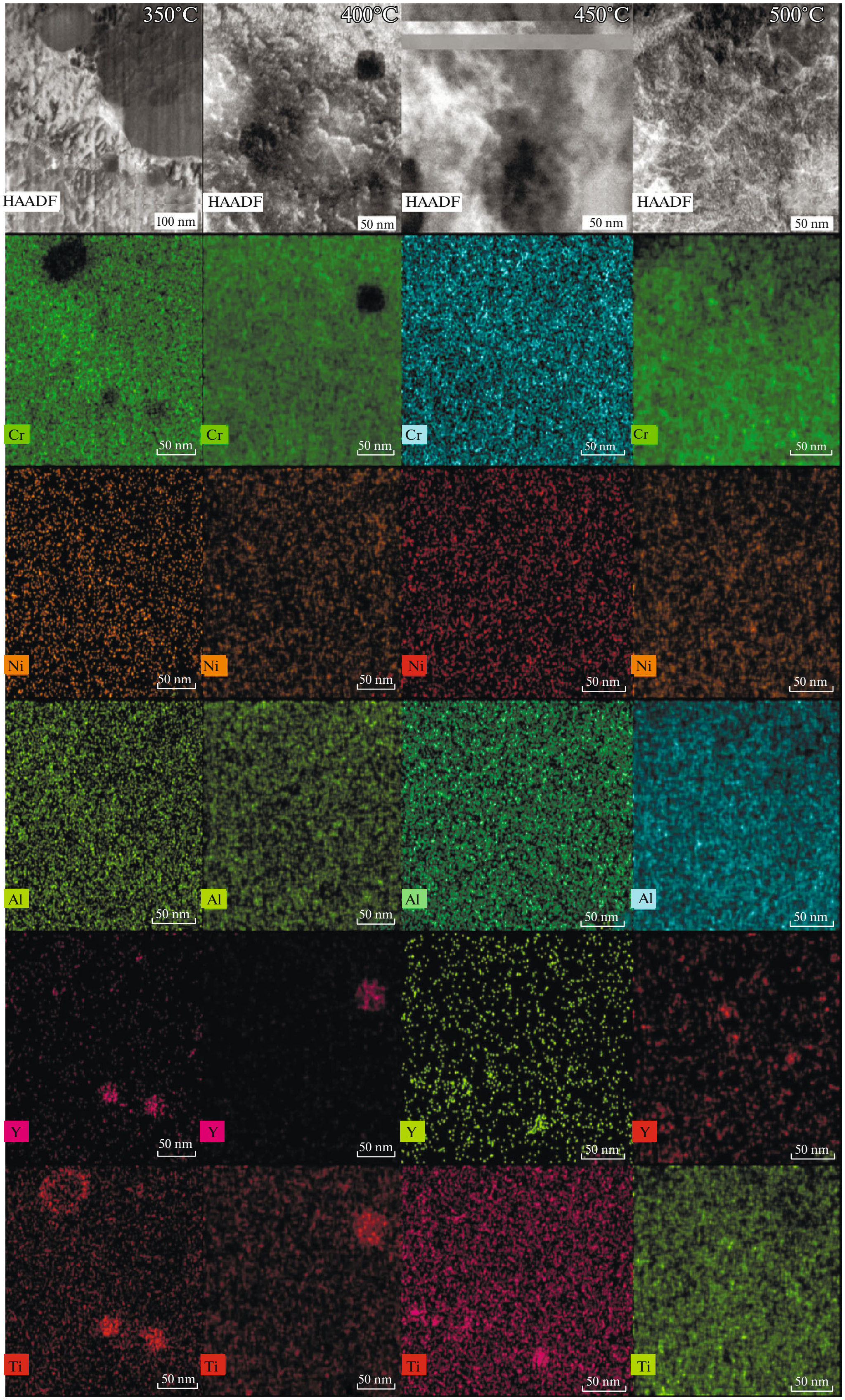

Fig. 12. Bright-field STEM images and corresponding EDX maps of chemical elements of the EP-450 DHO steel irradiated to 60 dpa at 350, 400, 450, and 500° (fluence of 1.7×10^{17} cm^{-2}, study at a depth of 0.5 μm from the irradiated surface).

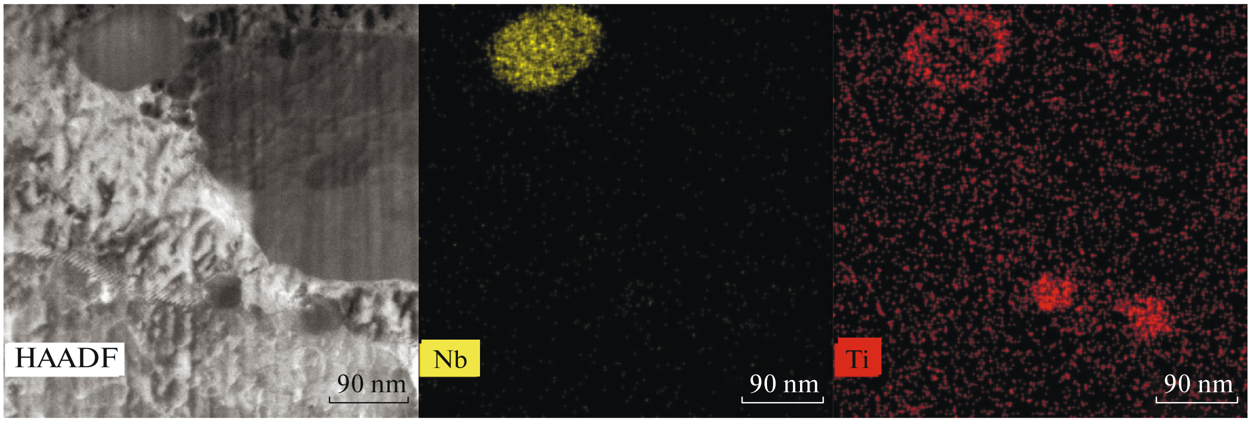

Fig. 13. Bright-field STEM image and EDX maps of Nb and Ti of the EP-823 DHO steel irradiated to 60 dpa at 350°C (fluence of 1.7×10^{17} cm^{-2}, study at a depth of 0.5 μm from the irradiated surface).

increase in temperature to 500°C, their enrichment in these elements increases.

After irradiation to 60 dpa at temperatures of 450°C and 500°C, clusters enriched in Cr and C were found. The presence of decomposition regarding Cr at high irradiation temperatures was noted by the STEM method, but it was not possible to conduct a quantitative analysis of this effect. Figure 20 shows the enrichment of Cr–C clusters relative to the matrix. The enrichment in Cr is tens of at % and in carbon is units of at %. Moreover, their enrichment in these elements increases with increasing temperature. The average size decreases from 8 to 4 nm, and the bulk density increases by an order of magnitude from 10^{22} to 10^{23} m^{-3} with increasing temperature (Figs. 16 and 18).

The characteristics of clusters in the EP-823 DHO steel upon irradiation are fundamentally different from those in the EP-450 DHO steel. A significant number of radiation-induced clusters of the Ni–Mn–Si type are detected after irradiation up to 30 dpa (Fig. 21). The average size of Ni–Mn–Si clusters ranges from 2 to 6 nm (Fig. 22a), and the bulk density varies from 10^{22} to 10^{23} m^{-3}. Figure 23 shows the enrichment of these clusters relative to the matrix.

A number of correlations between the characteristics of Ni–Mn–Si clusters and the irradiation parameters were found. At a temperature of 350°C at doses of 30 and 60 dpa, the bulk density of these clusters is 10^{23} m^{-3}, and a decrease in the density with increasing the dose is observed. At 100 dpa, the clusters were not included in the study area, which indicates that their bulk density is 10^{21} m^{-3} or lower.

At 400°C, with an increase in the irradiation dose, there is an increase in the average size of Ni–Mn–Si clusters from 2 to 5 nm with a simultaneous decrease in their bulk density. It should also be noted that the average cluster size does not depend much on the irradiation conditions and varies from 2 to 6 nm. One can talk about an increase in the cluster size at temperatures of 400 and 450°C, and it hardly changes at 350 and 500°C. The bulk density of clusters decreases with the dose at temperatures of 350 and 400°C; at 450°C, the density first increases and then decreases.

A detailed analysis of the composition of radiation-induced clusters shows that they are enriched not only in Ni, Mn, and Si but also in Cu (Fig. 24). With an increase in the irradiation temperature at 30 dpa, a tendency towards an increase in the enrichment of clusters in Cu and Mn is observed. In addition, there is an opposite effect at 60 dpa, the enrichment in these elements decreases.

Similar trends were not revealed in the enrichment of Si and Ni with an increase in temperature during irradiation to a dose of 30 dpa. The enrichment of clusters in Si varies from 5 to 14 at %. The enrichment of clusters in Ni varies from 10 to 18 at % at tempera-

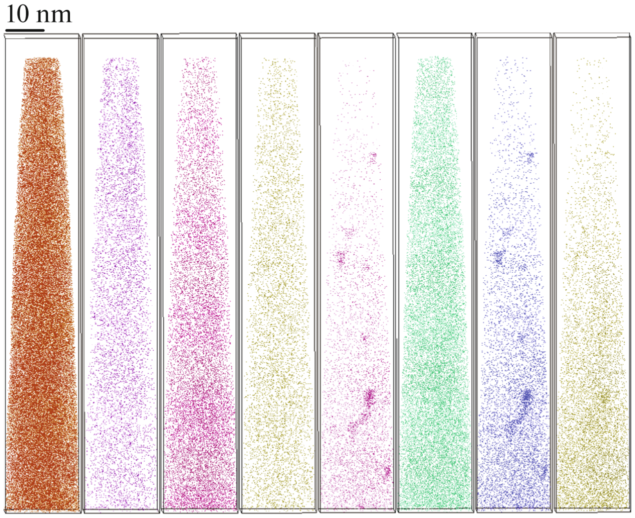

Fig. 14. Atomic maps of one of the bulks of the EP-450 DHO steel in the initial state.

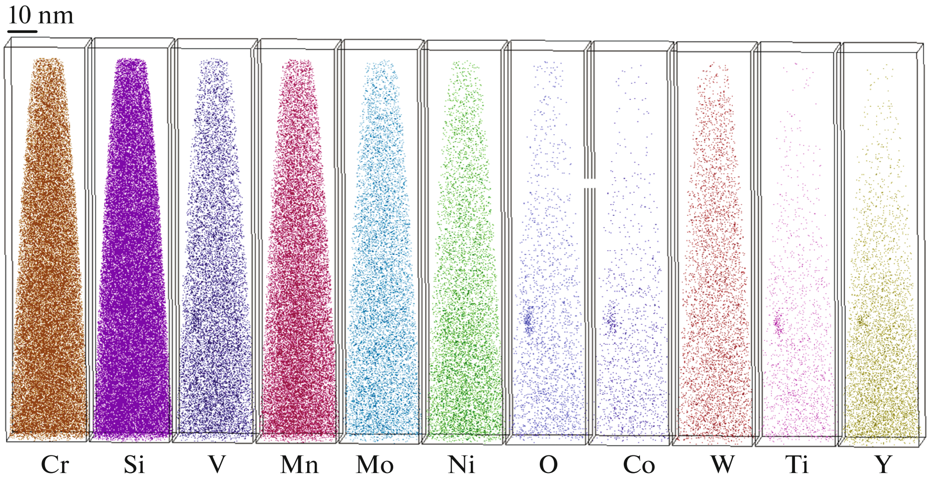

Fig. 15. Atomic maps of one of the bulks of the EP-823 DHO steel in the initial state.

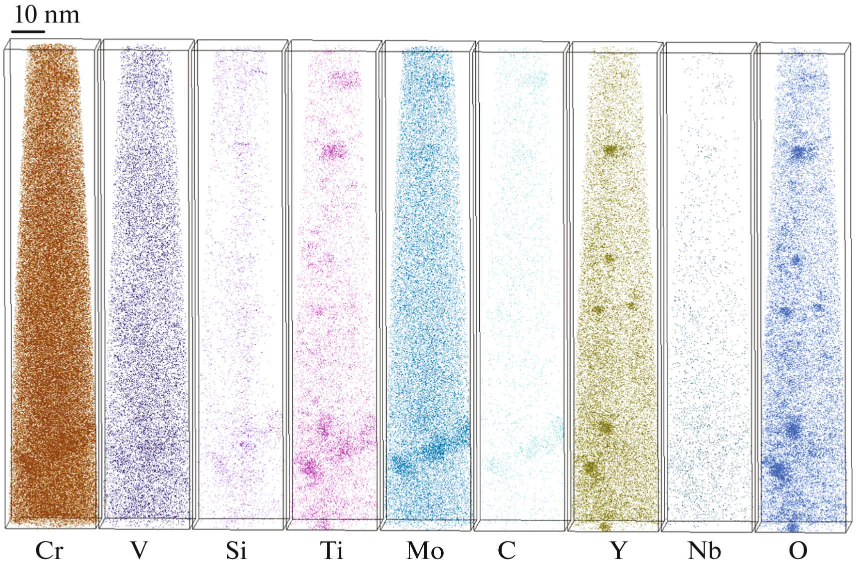

Fig. 16. Atomic maps of one of the bulks of the EP-450 DHO steel irradiated to 60 dpa at 400°C.

tures of 350, 400, and 450°C and increases sharply to 29 at % at 500°C.

After irradiation to 30 dpa at 450 and 500°C, radiation-induced clusters were found, predominantly enriched in Cu, with a size of 2–3 nm and a bulk density of 10^{22} m^{-3}. At 500°C, their bulk density drops by an order of magnitude (Fig. 25), compared to 450°C. The nature of these clusters is similar to Ni–Mn–Si clusters, since both types of clusters consist of the same elements, but in different proportions. The types of radiation-induced clusters found in EP823 DHO steel, in addition to different copper contents, differ greatly from each other in Ni and Si contents. It appears that Cu atoms displace Ni and Si in copper-rich clusters compared to Ni–Mn–Si clusters with a low copper content (Fig. 23).

Note that copper is a known element that promotes embrittlement of case materials, so even a small copper content leads to the formation of copper-rich radiation-induced clusters.

According to STEM data, after irradiation of EP823 DHO steel to doses of 60 and 100 dpa, dissolution of large oxide inclusions (≥10 nm) and formation of a new fraction of small inclusions (≤10 nm) are observed; also, this effect is more pronounced at high temperatures. This result is partially confirmed by the APT method. At an irradiation dose of 60 dpa and high irradiation temperatures (450 and 500°C), a large number of Y–Ti–Cr–O clusters are also detected

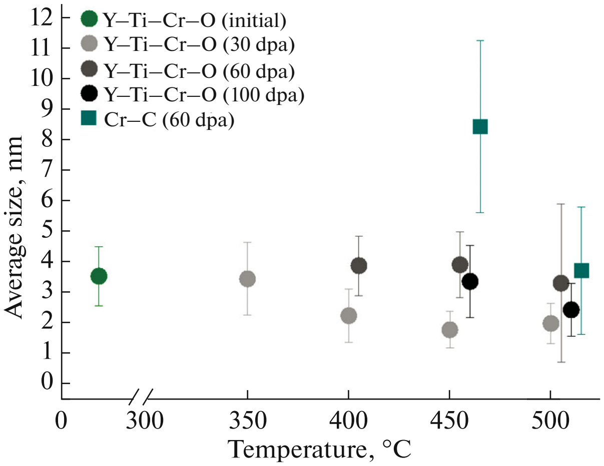

Fig. 17. Dependence of the average size of Y–Ti–Cr–O and Cr–C clusters on the irradiation temperature at damaging doses of 30, 60, and 100 dpa in the EP-450 DHO steel.

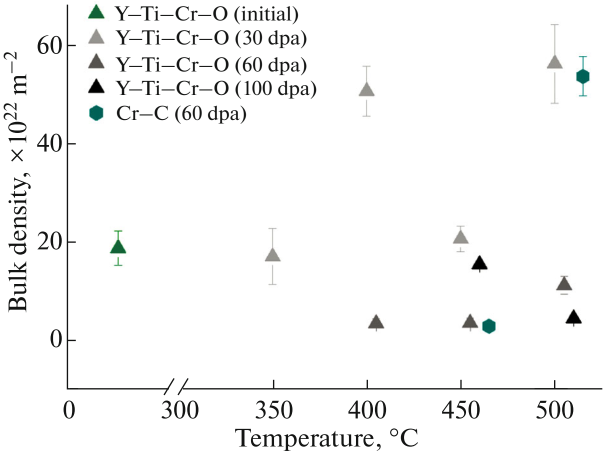

Fig. 18. Dependence of the bulk density of Y–Ti–Cr–O and Cr–C clusters on the irradiation temperature at damaging doses of 30, 60, and 100 dpa in the EP-450 DHO steel.

(Fig. 26). Moreover, at 500°C, their number is an order of magnitude higher than at 450°C and is 10^{22} m^{-3}, which is also evident from the results of TEM studies.

It is worth noting that, in the EP823 DHO steel, a noticeable number (~10^{22} m^{-3}) of Y–Ti–Cr–O clusters up to 6 nm in size, the low density of which (~10^{21} m^{-3}) was detected in the initial state, was found after irradiation to 30 dpa at 450°C, however, at 500°C, they did not fall into the APT study zone. This may be due to both the processes of cluster formation and dissolution and the heterogeneity of their distribution (10^{22} m^{-3}), since these values are at the threshold of the capabilities of detecting nanoobjects by APT methods.

After irradiation, these clusters have a different composition from the clusters in the initial state, which is indirectly confirmed by the STEM data, where small inclusions are found near large oxides. At 30 dpa, the enrichment in Cr, Ti, Y, and O increases by several times compared to the initial state. When irradiated to 60 dpa at 450°C, the enrichment of clusters in Ti and O does not change within the error limits compared to a similar temperature at 30 dpa, but the Cr content drops by 4 times, and Y increases by 4 times (Fig. 27). At 500°C, the enrichment in Y, Ti and O drops noticeably compared to 450°C for 60 dpa, but the enrichment in Cr increases by several times. This strong enrichment of clusters in Cr may be associated with the decomposition of the solid solution observed in the STEM (Fig. 12).

In addition to Y–Ti–Cr–O and Ni–Mn–Si clusters, after irradiation of EP-823 DHO steel to a dose of 100 dpa in the temperature range from 400 to 500°C, clusters of the Cr–C type were detected, as in the EP-450 DHO steel, but at 60 dpa. At this irradiation dose, decomposition regarding Cr was observed at high irradiation temperatures. The average size fluctuates from 4 to 10 nm with a bulk density of 10^{22} m^{-3}. With an increase in the irradiation temperature, the average size increases, and the bulk density decreases (Fig. 24). Figure 25 shows the enrichment of clusters relative to the matrix. The Cr content increases with increasing irradiation temperature with stable enrichment in C (Fig. 28a).

In addition to Cr and C, these clusters are enriched in Ni, Si, and Mn at 400°C. With increasing irradiation temperature, the composition changes. Enrichment in Mn is maintained. The Si content decreases at 450°C, and it completely leaves the clusters at 500°C, passing into a solid solution. Enrichment in Ni increases at 450°C, compared to 400°C, but at 500°C, nickel, like Si, leaves the clusters.

4. MEASUREMENT OF HARDENING OF ION-IRRADIATED STEELS BY NANOINDENTATION

Examples of the results of hardness measurements by the nanoindentation method are presented in the form of diagrams of hardness *H* versus the indentation depth *h* in Fig. 29.

Then the curves of hardness *H* versus the indentation depth *h* were reconstructed into a Nix–Gao diagram (H^2 versus $1/h$). Typical examples are shown in Fig. 30.

The resulting values of hardening of the DHO steels under irradiation at different temperatures are shown in Fig. 31.

The obtained results lie in the range from 0.4 to 1.4 GPa depending on the irradiation conditions.

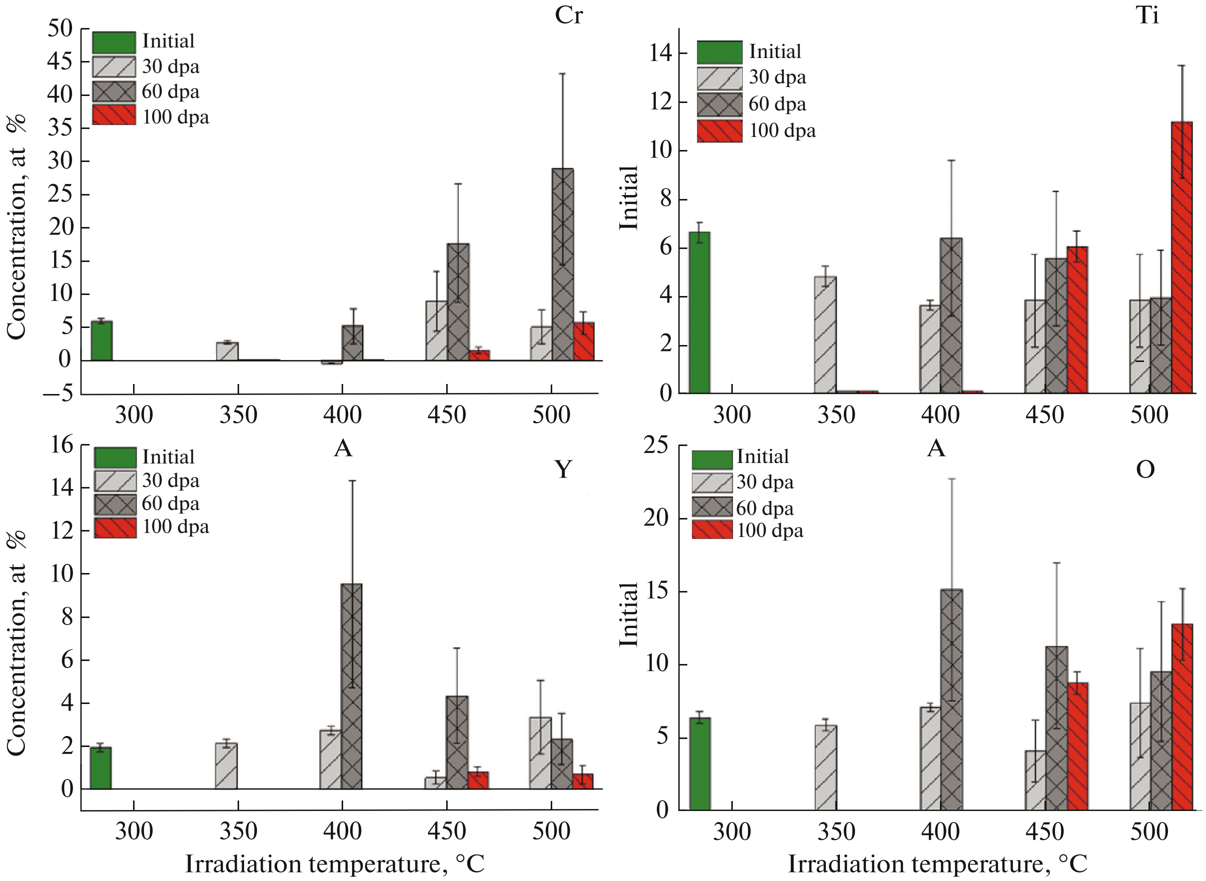

Fig. 19. Enrichment of Y–Ti–Cr–O clusters relative to the matrix after irradiation at damaging doses of 30, 60, and 100 dpa at different temperatures in the EP-450 DHO steel.

In the range of doses up to 30 dpa, the EP823 steel demonstrates a high rate of hardening; only at 500°C is a decrease in this rate observed. At higher doses, hardening decreases slightly at 350–450°C or stabilizes at 500°C. The EP-450 steel behaves differently up to 30 dpa; at low irradiation temperatures (350–400°C), the hardening rate is moderate, and at elevated temperatures (450–500°C), the hardening rate increases significantly.

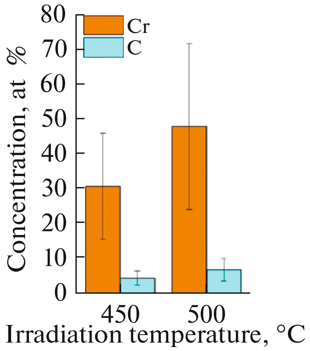

Fig. 20. Enrichment of Cr–C type clusters relative to the matrix after irradiation at a damaging dose of 60 dpa at different temperatures in the EP-450 DHO steel.

Analysis of the temperature dependences of hardening shows that, in the EP-823 DHO steel, hardening has some variations at temperatures of 350–450°C and drops significantly at 500°C. In the EP450 DHO steel, hardening increases slightly with temperature in the considered dose range up to 60 dpa and demonstrates a drop in hardening at 500°C only when irradiated up to 100 dpa.

5. DISCUSSION

The mechanisms of radiation hardening of DHO steels, as a rule, have a combined nature. On the hand, the matrix of these steels can demonstrate the radiation effects of the matrix steel. For example, in traditional ferritic-martensitic steels, the main mechanisms of low-temperature radiation hardening are formation of dislocation loops and radiation-induced clusters (such as Ni-Mn-Si clusters or Cu clusters, depending on the composition of the steels) [50–53]. In modern low-activation ferritic-martensitic steels, the content of Ni, Si, Mn, and Cu is so well optimized

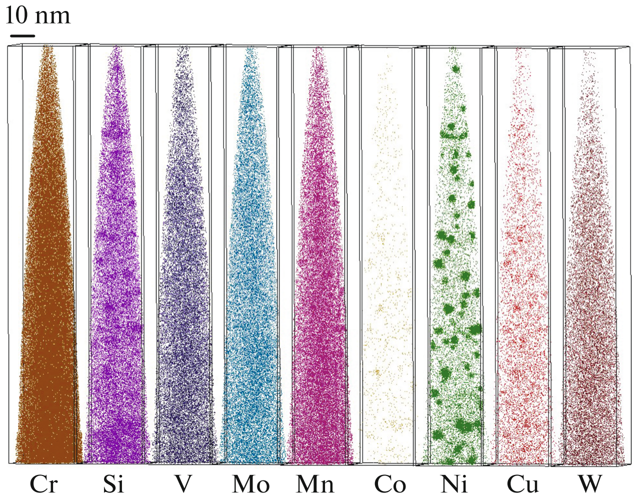

Fig. 21. Atomic maps of the EP-823 DHO steel after irradiation to a dose of 60 dpa at a temperature of 350°C.

that the mentioned clusters are hardly formed; however, at higher irradiation doses, decomposition of the solid solution regarding Cr and the formation of preprecipitates of the α' phase are still possible [54–56]. On the other hand, the presence of a high density of dispersed inclusions can suppress the noted mechanisms of decomposition of the solid solution of the matrix steel and suppress the formation of dislocation loops [57], at least in the initial stages of irradiation. In this case, irradiation leads, first of all, to the restructuring of the system of dispersed inclusions, for example, to the exchange of matter between oxide inclusions and clusters, the dissolution of large oxides, and the formation of new nanosized oxide inclusions [30–32, 57].

In this paper, the mechanisms of radiation hardening of two DHO steels EP450 DHO and EP823 DHO have been studied, which have not only noticeable differences in chemical composition (EP823 DHO steel has significantly more Mn, Ni, Si and W) but also different degrees of dispersion of nanoobjects.

Analysis of the initial state of the steels showed that EP450 DHO and EP-823 DHO contain a relatively low oxide density of ~2–4 × 10^{21} m^{-3}, compared to known foreign model steels and alloys [22], which have an oxide density of more than 10^{22} m^{-3}. At the same time, the oxide particles in the EP450 DHO steel have a smaller average size (10 nm) and a higher bulk density (~3 × 10^{21} m^{-3}) compared to the EP823 DHO steel, where these values are 15 nm and ~2 × 10^{21} m^{-3}, respectively (Table 2). In the EP450 DHO and EP823 DHO steels, nanosized (<5 nm) Y–Ti–Cr–O clusters are also found, but in the EP450 DHO steel, there are two orders of magnitude more such clusters (~10^{23} m^{-3}) than in the EP823 DHO steel. It should be noted that the low cluster density of ~10^{21} m^{-3} is also not typical of DHO steels [19, 22].

Differences in the initial nanostructure of the steels manifested themselves in the difference in their behavior under radiation loads.

The EP-450 DHO steel is quite highly dispersed. Thus, at low irradiation doses (up to 30 dpa), noticeable processes of rearrangement of the system of inclusions (oxides and clusters) were detected. But the processes of decomposition of the solid solution for Cr were detected only at high irradiation doses (60 dpa) and at sufficiently high irradiation temperatures. It should be noted that, despite the high dispersion of the

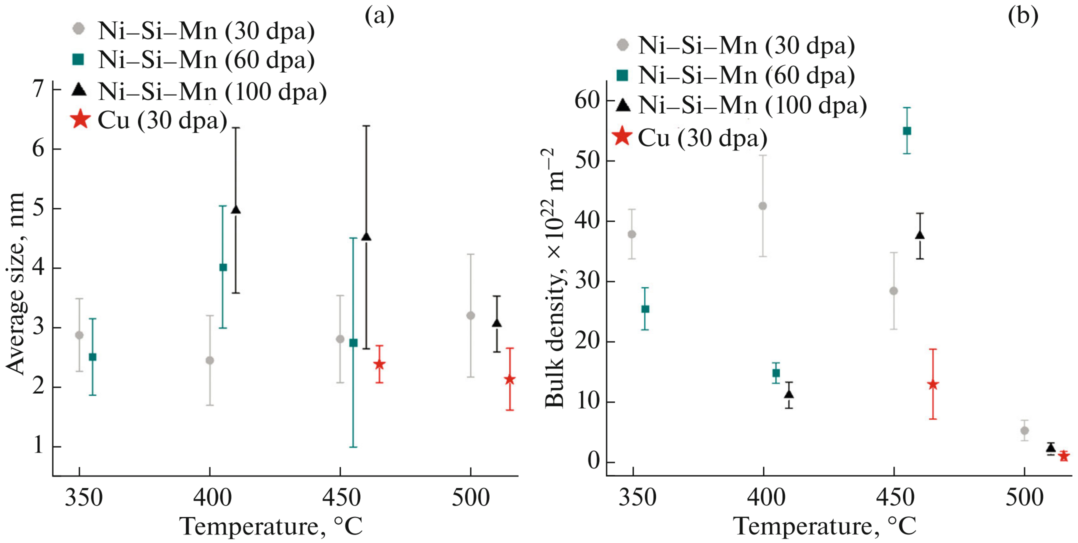

Fig. 22. Dependence of the (a) average size and (b) bulk density of Ni–Mn–Si clusters and Cu clusters on the irradiation temperature at damaging doses of 30, 60, and 100 dpa in the EP-823 DHO steel.

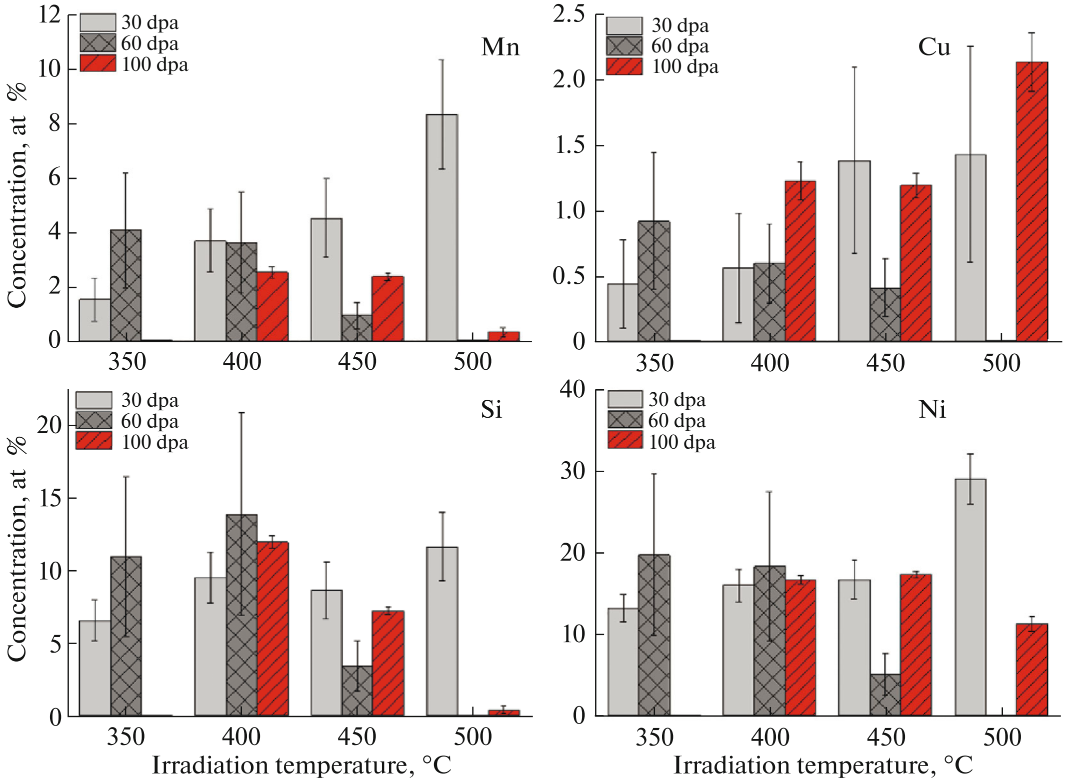

Fig. 23. Enrichment of Ni–Mn–Si type clusters relative to the matrix after irradiation at damaging doses of 30, 60, and 100 dpa at different temperatures in the EP-823 DHO steel.

nanophases of this steel, the formation of dislocation loops was not suppressed, and they were detected already at a dose of 30 dpa.

Oxides and clusters in the EP823 DHO steel have a lower dispersion, in comparison with the EP450 DHO. The lower density of oxides and extremely low density of oxide clusters allowed the mechanisms of matrix steel degradation to manifest themselves. The Ni, Si, and Mn content typical of traditional ferritic-martensitic steels led to the intense formation of Ni–Si–Mn clusters (~10^{23} m^{-3}) and copper-rich clusters, despite the low copper content in the material (less than 0.1%). As the radiation dose increased, against the background of the coalescence of the formed clusters, the processes of restructuring of oxide inclusions also manifested themselves in the EP823 DHO steel.

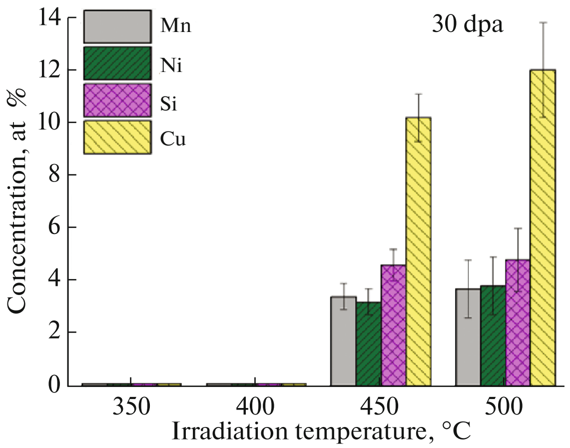

Fig. 24. Enrichment of Cu clusters relative to the matrix after irradiation at damaging doses of 30, 60, and 100 dpa at different temperatures in the EP-823 DHO steel.

Dislocation loops in the EP-823 DHO steel have parameters close to those in the EP450 DHO steel. It can be assumed that, in this case, the relatively low rate of dislocation loop formation is associated with the intense formation of radiation-induced clusters.

The noted features of the rearrangement of the nanostructure of steels determined the detected differences in the radiation hardening of these steels.

Thus, the EP-823 DHO steel has a significantly higher rate of low-temperature radiation hardening in the dose range of up to 30 dpa, unlike EP450 DHO steel. An increase in the radiation dose in the case of the EP823 DHO steel leads to gradual softening. Moreover, this effect has a temperature dependence: for each radiation dose, an increase in temperature leads to softening.

The behavior of the EP450 DHO steel is characterized by the fact that an increase in the dose does not

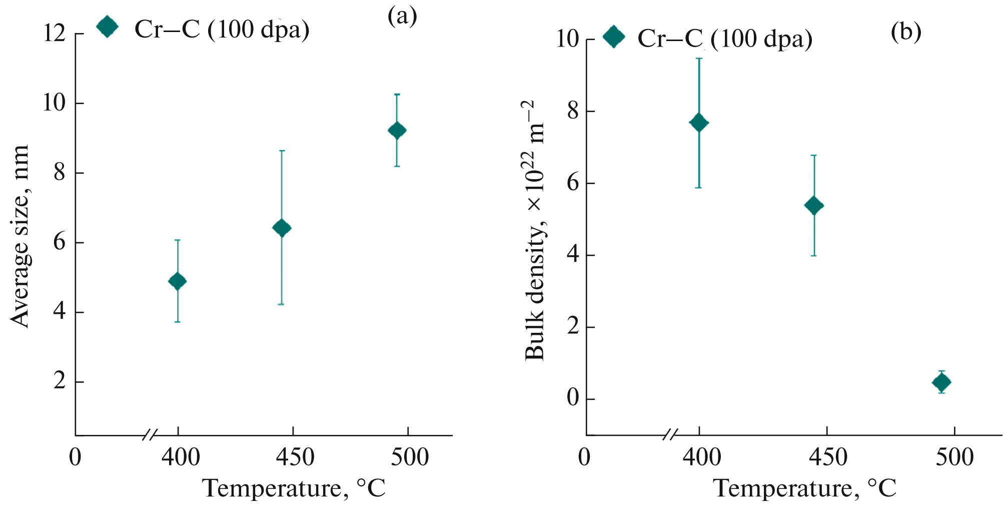

Fig. 25. Dependence of the (a) average size and (b) bulk density of Y–Ti–Cr–O and Cr–C clusters on the irradiation temperature at damaging doses of 30, 60, and 100 dpa in the EP-823 DHO steel.

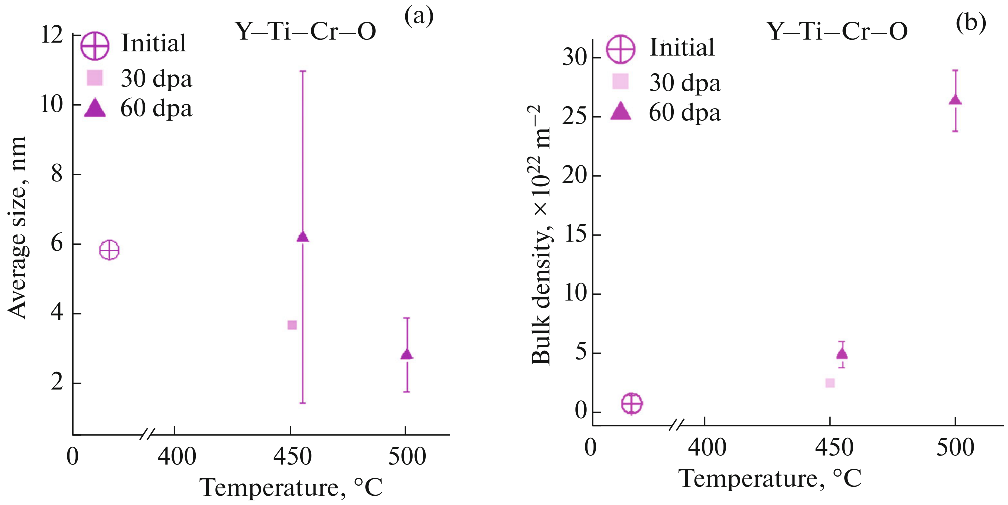

Fig. 26. Dependence of the (a) average size and (b) bulk density of Y–Ti–Cr–O and Cr–C clusters on the irradiation temperature at damaging doses of 30, 60, and 100 dpa in the EP-823 DHO steel.

lead to softening, as in the case of the EP823 DHO: at a dose of 60 dpa, EP450 DHO steel hardens, and this hardening increases with increasing temperature. At a dose of 100 dpa, the trend changes, and the EP450 DHO steel demonstrates softening. This effect is more pronounced at high temperatures (450 and 500°C).

The differences in the behavior of mechanical properties of the two steels are directly related to the reorganization of their microstructure and nanostructure. Some effects are quite obvious in terms of their description by changes in the microstructure and nanostructure. For example, the higher hardening rate of the EP823 DHO steel, in contrast to the EP450 DHO, is most likely associated with the formation of a large number of radiation-induced Ni–Si–Mn clusters in the EP823 DHO. It can be also assumed that since the nanostructured phases in the EP823 DHO steel have a lower dispersion than in the EP450 DHO steel, the effect of oxide inclusions on the resulting hardening is less, and radiation hardening is largely determined by changes in the characteristics of dislocation loops, as in the case of conventional ferritic-martensitic steel.

For the EP450 DHO steel, the situation is completely different. Although dislocation loops have similar characteristics and demonstrate similar behavior under irradiation, as in the case of the EP823 DHO steel, the nanostructure of EP450 DHO steel, having a significantly greater dispersion, has a significantly greater influence of oxide inclusions of various types

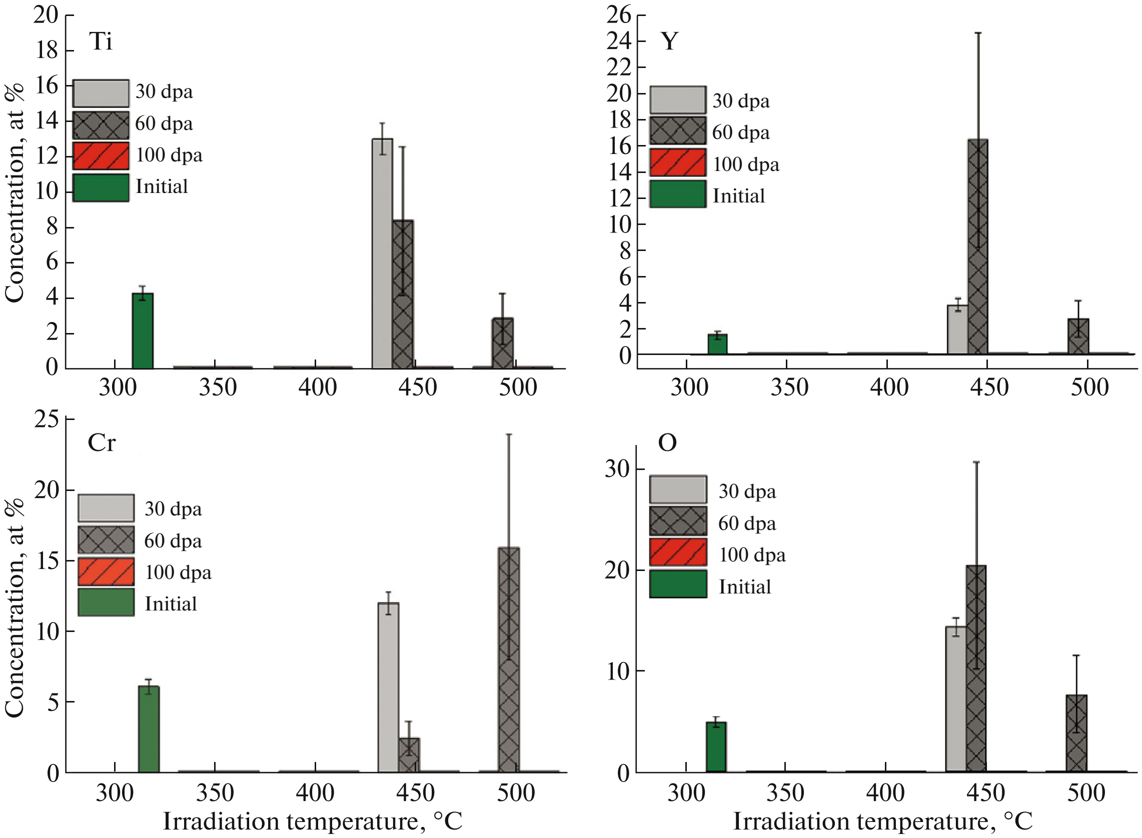

Fig. 27. Enrichment of Y–Ti–Cr–O clusters relative to the matrix after irradiation at damaging doses of 30, 60, and 100 dpa at different temperatures in the EP-823 DHO steel.

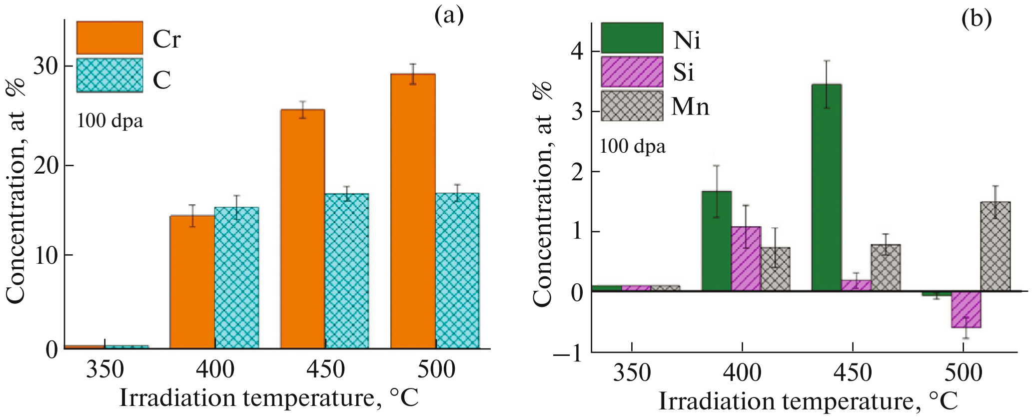

Fig. 28. Enrichment of Cr–C clusters relative to the matrix after irradiation at damaging doses of 30, 60, and 100 dpa at different temperatures in the EP-823 DHO steel.

on the resulting radiation hardening, and this is manifested at high irradiation doses.

CONCLUSIONS

In this paper, the nanostructure of two ferritic-martensitic steels EP823 DHO and EP450 DHO and their evolution after simulated irradiation with ions in the dose range from 30 to 100 dpa, at irradiation temperatures from 350 to 500°C, were studied using transmission electron microscopy and atomic probe tomography.

Analysis of the initial state of the steels showed that the EP450 DHO steel contained a larger number of

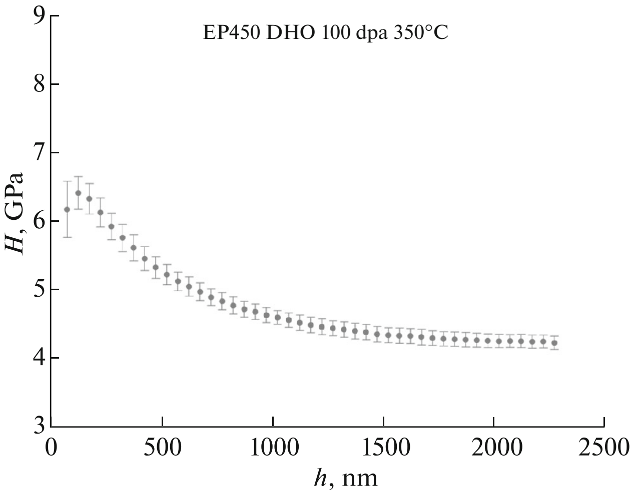

Fig. 29. Dependence of the hardness on indentation depth for the EP-450 DHO steel sample after irradiation.

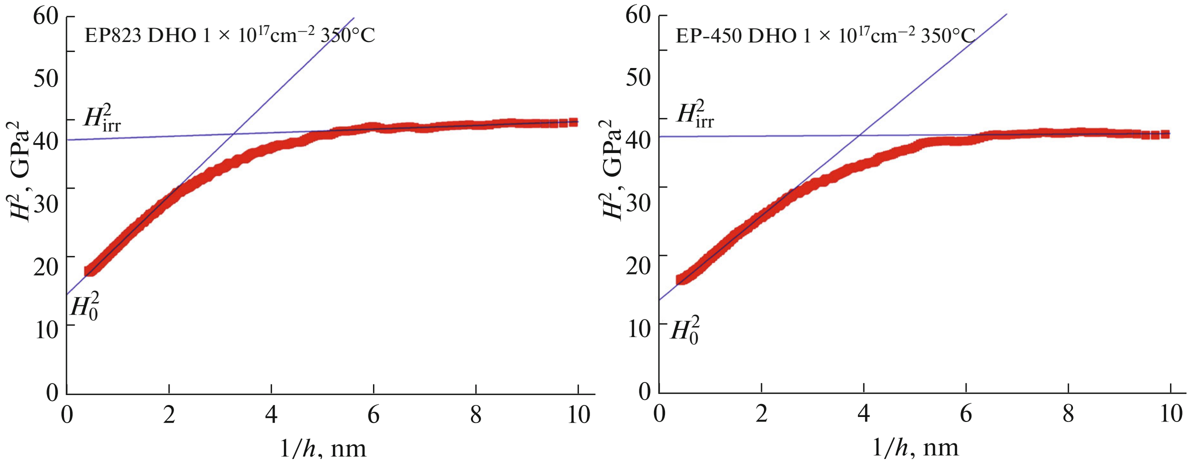

Fig. 30. Diagram of measured hardness values versus the depth for the (a) EP-450 DHO and (b) EP-823 DHO steel irradiated with ions at a temperature of 350°C in the coordinates of H^2 versus $1/h$.

small oxide particles (up to 20 nm) compared to the EP-823 DHO steel. In addition, the EP450 DHO steel contained two orders of magnitude more (~10^{23} m^{-3}) nanosized Y–Ti–Cr–O clusters than the EP823 DHO steel.

After irradiation to a dose of 30 dpa, the evolution of the nanostructure of the steels occurs in different ways. In the EP823 DHO steel, a large number of thermally unstable radiation-induced clusters enriched in Ni, Mn, Si and Cu are formed. The bulk density of the initial small oxides noticeably decreases after irradiation. In the EP450 DHO steel, radiation-induced clusters, as in the EP823 DHO steel, are not found. The average values of the sizes and densities of oxide particles change insignificantly.

At higher irradiation doses (60 and 100 dpa), both steels show signs of solid solution decomposition regarding Cr. Changes in the quantitative characteristics of oxides are insignificant for the EP450 DHO steel. The detected Cr–Y–Ti–O clusters in the initial state for this steel are also present in the vast majority of the states after irradiation. At the same time, the clusters are less stable to high irradiation doses than oxide particles.

In the EP823 DHO steel, after irradiation to 60 and 100 dpa, the bulk densities of oxide particles increase. At the same time, at high irradiation temperatures, their gradual dissolution is observed (a decrease in the bulk density, a shift in distributions towards smaller sizes).

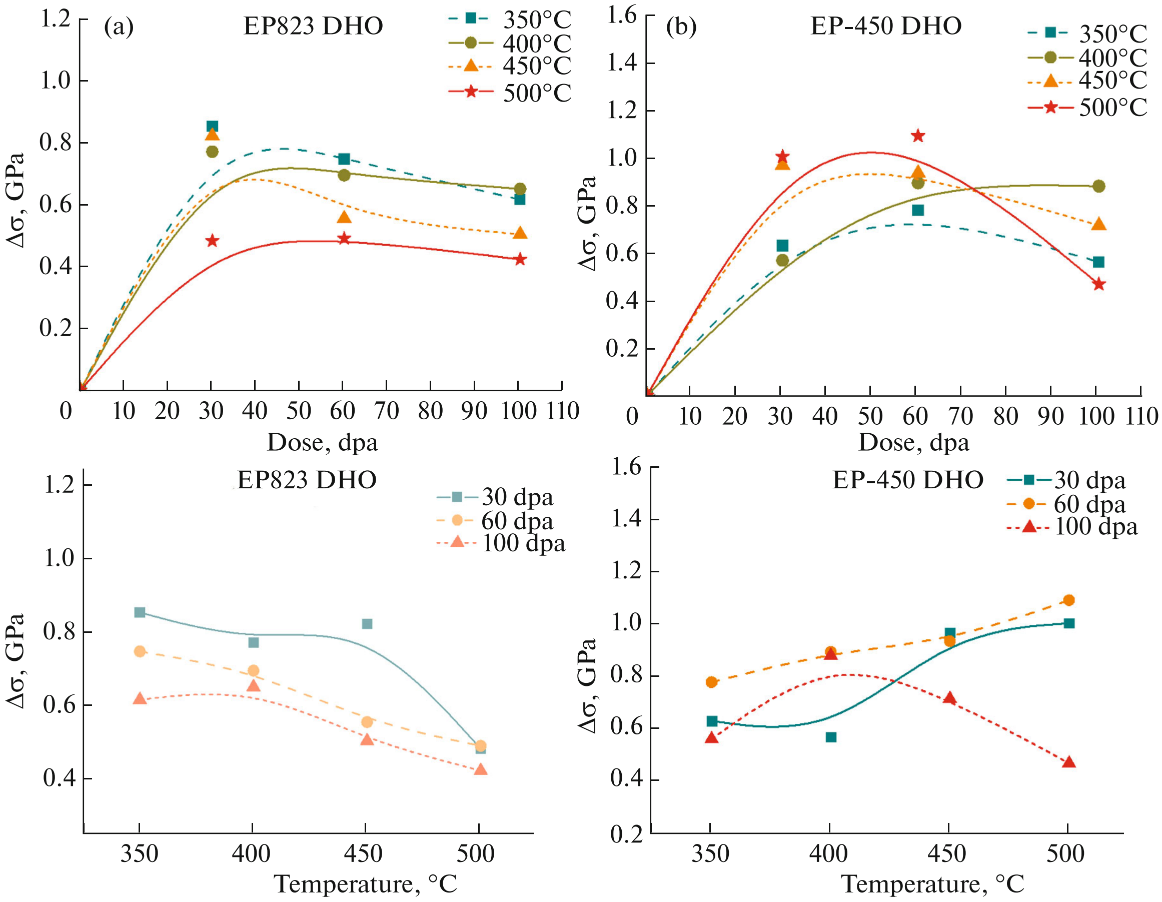

Fig. 31. Hardening of the (a) EP-450 DHO and (b) EP-823 DHO steels as a result of ion irradiation.

The results of nanohardness measurements show that the main differences in the behavior of the two steels occur at high temperatures after irradiation to doses of 30 and 60 dpa. The EP450 DHO steel is more stable to ion irradiation up to doses of 100 dpa in the temperature range from 350°C to 500°C. At a dose of 100 dpa, both steels show a tendency to soften with increasing temperature.

ACKNOWLEDGMENTS

The work was carried out on the equipment of the Center for Collective Use KAMIKS (http://kamiks.itep.ru/) of the National Research Center Kurchatov Institute—Kurchatov Complex of Theoretical and Experimental Physics.

FUNDING

This work was supported by ongoing institutional funding. No additional grants to carry out or direct this particular research were obtained.

CONFLICT OF INTEREST

The authors of this work declare that they have no conflicts of interest.

REFERENCES

1. Sh. Ukai and M. Fujiwara, J. Nucl. Mater. **307–311**, 749 (2002). https://doi.org/10.1016/s0022-3115(02)01043-7
2. A. A. Nikitina, V. S. Ageev, M. V. Leont'eva-Smirnova, N. M. Mitrofanova, I. A. Naumenko, A. V. Tselishchev, and V. M. Chernov, At. Energy **119**, 362 (2016). https://doi.org/10.1007/s10512-016-0074-2
3. S. Ukai, S. Ohtsuka, T. Kaito, Y. De Carlan, J. Ribis, and J. Malaplate, in *Structural Materials for Generation IV Nuclear Reactors*, Ed. by P. Yvon (Elsevier, 2017), p. 357. https://doi.org/10.1016/b978-0-08-100906-2.00010-0
4. Y. De Carlan, J.-L. Bechade, P. Dubuisson, J.-L. Seran, P. Billot, A. Bougault, T. Cozzika, S. Doriot, D. Hamon, J. Henry, M. Ratti, N. Lochet, D. Nunes, P. Olier, T. Leblond, and M. H. Mathon, J. Nucl. Mater. **386–388**, 430 (2009). https://doi.org/10.1016/j.jnucmat.2008.12.156
5. P. Yvon and F. /. Carré, J. Nucl. Mater. **385**, 217 (2009). https://doi.org/10.1016/j.jnucmat.2008.11.026
6. Yo. H. Jeong, W. J. Kim, D. J. Kim, J. Jang, S. H. Kang, Y.-B. Chun, and T. K. Kim, Procedia Eng. **86**, 1 (2014). https://doi.org/10.1016/j.proeng.2014.11.004
7. R. Mateus, P. A. Carvalho, D. Nunes, L. C. Alves, N. Franco, J. B. Correia, and E. Alves, Fusion Eng.

Des. **86**, 2386 (2011).
https://doi.org/10.1016/j.fusengdes.2011.01.011

8. A. Kimura, H.-S. Cho, N. Toda, R. Kasada, K. Yutani, H. Kishimoto, N. Iwata, Sh. Ukai, and M. Fujiwara, J. Nucl. Sci. Technol. **44**, 323 (2007). https://doi.org/10.1080/18811248.2007.9711289
9. J. Ribis, E. Bordas, P. Trocellier, Yv. Serruys, Ya. De Carlan, and A. Legris, J. Mater. Res. **30**, 2210 (2015). https://doi.org/10.1557/jmr.2015.183
10. J. P. Wharry, M. J. Swenson, and K. H. Yano, J. Nucl. Mater. **486**, 11 (2017). https://doi.org/10.1016/j.jnucmat.2017.01.009
11. M. Klimiankou, R. Lindau, and A. Möslang, J. Nucl. Mater. **329–333**, 347 (2004). https://doi.org/10.1016/j.jnucmat.2004.04.083
12. M. Klimiankou, R. Lindau, and A. Möslang, J. Cryst. Growth **249**, 381 (2003). https://doi.org/10.1016/s0022-0248(02)02134-6
13. V. S. Ageev, N. F. Vil'danova, K. A. Kozlov, T. N. Kochetkova, A. A. Nikitina, V. V. Sagaradze, B. V. Safronov, V. V. Tsvelev, and A. P. Chukanov, Phys. Met. Metallogr. **106**, 318 (2008). https://doi.org/10.1134/s0031918x08090123
14. R. Coppola, M. Klimiankou, R. Lindau, R. P. May, and M. Valli, Phys. B: Condens. Matter **350**, E545 (2004). https://doi.org/10.1016/j.physb.2004.03.148
15. Y.-S. Han, X. Mao, J. Jang, and T.-K. Kim, Appl. Phys. A **119**, 249 (2015). https://doi.org/10.1007/s00339-014-8956-4
16. M. H. Mathon, M. Perrut, S. Y. Zhong, and Y. De Carlan, J. Nucl. Mater. **428**, 147 (2012). https://doi.org/10.1016/j.jnucmat.2011.12.010
17. N. Oono and Sh. Ukai, Mater. Trans. **59**, 1651 (2018). https://doi.org/10.2320/matertrans.m2018110
18. S. V. Rogozhkin, Yu. E. Gorshkova, G. D. Bokuchava, A. A. Khomich, A. A. Bogachev, and A. A. Nikitin, Phys. At. Nucl. **85**, 1467 (2022) [S. V. Rogozhkin et al., Yad. Fiz. Inzhin. **13** (4), 317 (2022)]. https://doi.org/10.1134/S1063778822090290
19. S. V. Rogozhkin, A. A. Khomich, A. V. Klauz, A. A. Bogachev, Y. E. Gorshkova, G. D. Bokuchava, A. A. Nikitin, A. A. Lukyanchuk, O. A. Raznitsyn, A. S. Shutov, and A. G. Zaluzhny, J. Surf. Invest.: X-ray, Synchrotron Neutron Tech. **16**, 1189 (2022). https://doi.org/10.1134/s1027451022060490
20. C. A. Williams, E. A. Marquis, A. Cerezo, and G. D. W. Smith, J. Nucl. Mater. **400**, 37 (2010). https://doi.org/10.1016/j.jnucmat.2010.02.007
21. M. K. Miller, D. T. Hoelzer, E. A. Kenik, and K. F. Russell, J. Nucl. Mater. **329–333**, 338 (2004). https://doi.org/10.1016/j.jnucmat.2004.04.085
22. S. V. Rogozhkin, A. A. Khomich, A. A. Bogachev, A. A. Nikitin, A. A. Lukyanchuk, O. A. Raznitsyn, A. S. Shutov, A. L. Vasiliev, and M. Yu. Presniakov, Phys. At. Nucl. **83**, 1425 (2020) [S. V. Rogozhkin et al., Yad. Fiz. Inzhin. **11** (1), 22 (2020)]. https://doi.org/10.1134/S1063778820100191
23. A. J. London, S. Santra, S. Amirthapandian, B. K. Panigrahi, R. M. Sarguna, S. Balaji, R. Vijay, C. S. Sundar, S. Lozano-Perez, and C. R. M. Grovenor, Acta Mater. **97**, 223 (2015). https://doi.org/10.1016/j.actamat.2015.06.032
24. B. van der Schaaf, F. Tavassoli, C. Fazio, E. Rigal, E. Diegele, R. Lindau, and G. LeMarois, Fusion Eng. Des. **69**, 197 (2003). https://doi.org/10.1016/S0920-3796(03)00337-5
25. R. Lindau, A. Möslang, M. Rieth, M. Klimiankou, E. Materna-Morris, A. Alamo, A. Tavassoli, C. Cayron, A.-M. Lancha, P. Fernandez, N. Baluc, R. Schäublin, E. Diegele, G. Filacchioni, J. W. Rensman, B. van der Schaaf, E. Lucon, and W. Dietz, Fusion Eng. Des. **75–79**, 989 (2005). https://doi.org/10.1016/j.fusengdes.2005.06.186
26. M. Klimenkov, R. Lindau, and A. Möslang, J. Nucl. Mater. **386–388**, 553 (2009). https://doi.org/10.1016/j.jnucmat.2008.12.174
27. S. V. Rogozhkin, A. V. Klauz, Yu. Ke, L. Almásy, A. A. Nikitin, A. A. Khomich, A. A. Bogachev, Yu. E. Gorshkova, G. D. Bokuchava, G. P. Kopitsa, and L. Sun, Nanomaterials **14**, 194 (2024). https://doi.org/10.3390/nano14020194
28. R. L. Klueh, J. P. Shingledecker, R. W. Swindeman, and D. T. Hoelzer, J. Nucl. Mater. **341**, 103 (2005). https://doi.org/10.1016/j.jnucmat.2005.01.017
29. Sh. Ukai, T. Okuda, M. Fujiwara, T. Kobayashi, S. Mizuta, and H. Nakashima, J. Nucl. Sci. Technol. **39**, 872 (2002). https://doi.org/10.1080/18811248.2002.9715271
30. S. Rogozhkin, A. Bogachev, O. Korchuganova, A. Nikitin, N. Orlov, A. Aleev, A. Zaluzhnyi, M. Kozodaev, T. Kulevoy, B. Chalykh, R. Lindau, J. Hoffmann, A. Möslang, P. Vladimirov, M. Klimenkov, M. Heilmaier, J. Wagner, and S. Seils, Nucl. Mater. Energy **9**, 66 (2016). https://doi.org/10.1016/j.nme.2016.06.011
31. S. V. Rogozhkin, A. A. Khomich, A. A. Bogachev, A. A. Nikitin, V. V. Khoroshilov, T. V. Kulevoy, P. A. Fedin, K. E. Pryanishnikov, A. A. Lukyanchuk, O. A. Raznitsyn, A. S. Shutov, A. G. Zaluzhnyi, A. L. Vasiliev, and M. Yu. Presniakov, Phys. At. Nucl. **83**, 1519 (2020) [S. V. Rogozhkin et al., Yad. Fiz. Inzhin. **11** (2), 67 (2020)]. https://doi.org/10.1134/S1063778820100208
32. S. V. Rogozhkin, A. V. Klauz, A. A. Bogachev, A. A. Khomich, P. A. Fedin, and O. A. Raznitsyn, J. Surf. Invest.: X-ray, Synchrotron Neutron Tech. **17**, S289 (2023). https://doi.org/10.1134/S1027451023070443
33. A. A. Nikitina, V. S. Ageev, A. P. Chukanov, V. V. Tsvelev, N. P. Porezanov, and O. A. Kruglov, J. Nucl. Mater. **428**, 117 (2012). https://doi.org/10.1016/j.jnucmat.2012.02.022
34. A. A. Nikitina, E. V. Tsvetkova, and K. A. Ivanov, Vopr. At. Nauki Tekh., Ser.: Materialoved. Nov. Mater., No. 4, 30 (2018).
35. S. V. Rogozhkin, A. A. Nikitin, A. A. Khomich, N. A. Iskandarov, V. V. Khoroshilov, A. A. Bogachev, A. A. Lukyanchuk, O. A. Raznitsyn, A. S. Shutov, P. A. Fedin, R. P. Kuibeda, T. V. Kulevoy, A. L. Vasiliev, M. Yu. Presniakov, K. S. Kravchuk, and A. S. Useinov, Phys. At. Nucl. **82**, 1239 (2019) [S. V. Rogozhkin et al., Yad. Fiz. Inzhin. **9** (3), 245

(2018)].
https://doi.org/10.1134/S1063778819090072

36. P. A. Fedin, M. S. Saratovskikh, R. P. Kuibeda, A. L. Sitnikov, T. V. Kulevoy, A. A. Nikitin, and S. V. Rogozhkin, J. Phys.: Conf. Ser. **1115**, 032026 (2018).
https://doi.org/10.1088/1742-6596/1115/3/032026
37. G. N. Kropachev, R. P. Kuibeda, A. I. Semennikov, A. A. Aleev, A. D. Fertman, T. V. Kulevoy, A. A. Nikitin, S. V. Rogozhkin, and M. Cavenago, in *Proc. HIAT09* (Venice, 2009), p. 236.
38. S. V. Rogozhkin, A. A. Nikitin, A. A. Khomich, N. A. Iskandarov, V. V. Khoroshilov, A. A. Bogachev, A. A. Lukyanchuk, O. A. Raznitsyn, A. S. Shutov, T. V. Kulevoy, P. A. Fedin, A. L. Vasiliev, and M. Yu. Presnyakov, Inorg. Mater.: Appl. Res. **10**, 333 (2019).
https://doi.org/10.1134/S2075113319020357
39. S. Taller, G. Vancoevering, B. D. Wirth, and G. S. Was, Sci. Rep. **11**, 2949 (2021).
https://doi.org/10.1038/s41598-021-82512-w
40. J. F. Ziegler, M. D. Ziegler, and J. P. Biersack, Nucl. Instrum. Methods Phys. Res., Sect. B **268**, 1818 (2010).
https://doi.org/10.1016/j.nimb.2010.02.091
41. S. V. Rogozhkin, A. A. Aleev, A. A. Lukyanchuk, A. S. Shutov, O. A. Raznitsyn, and S. E. Kirillov, Instrum. Exp. Tech. **60**, 428 (2017).
https://doi.org/10.1134/S002044121702021x
42. A. A. Aleev, S. V. Rogozhkin, A. A. Luk'yanchuk, A. S. Shutov, O. A. Raznitsyn, A. A. Nikitin, N. A. Iskandarov, O. A. Korchuganova, and S. E. Kirillov, RF Certificate of State Registration of Software No. 2018661876, Byull. Izobret., No. 9 (2018).
https://www.elibrary.ru/flcvjk.
43. P. Bas, A. Bostel, B. Deconihout, and D. Blavette, Appl. Surf. Sci. **87–88**, 298 (1995).
https://doi.org/10.1016/0169-4332(94)00561-3
44. A. A. Lukyanchuk, A. A. Aleev, A. S. Shutov, O. A. Raznitsyn, C. E. Kirillov, and S. V. Rogozhkin, Phys. At. Nucl. **84**, 1836 (2021) [A. A. Lukyanchuk et al., Yad. Fiz. Inzhin. **13** (1), 272 (2022)].
https://doi.org/10.1134/S1063778821120048
45. A. S. Shutov, A. A. Lukyanchuk, S. V. Rogozhkin, O. A. Raznitsyn, A. A. Nikitin, A. A. Aleev, and S. E. Kirillov, Phys. At. Nucl. **82**, 1292 (2019) [A. S. Shutov et al., Yad. Fiz. Inzhin. 9 (4), 371 (2018)].
https://doi.org/10.1134/S1063778819090096
46. X. Li and B. Bhushan, Mater. Charact. **48**, 11 (2002).
https://doi.org/10.1016/s1044-5803(02)00192-4
47. W. D. Nix and H. Gao, J. Mech. Phys. Solids **46**, 411 (1998).
https://doi.org/10.1016/s0022-5096(97)00086-0
48. I. Manika, J. Maniks, and K. Schwartz, J. Phys. D: Appl. Phys. **41**, 074008 (2008).
https://doi.org/10.1088/0022-3727/41/7/074008
49. L. Qian, M. Li, Zh. Zhou, H. Yang, and X. Shi, Surf. Coat. Technol. **195**, 264 (2005).
https://doi.org/10.1016/j.surfcoat.2004.07.108
50. Z. Jiao, S. Taller, K. Field, G. Yeli, M. P. Moody, and G. S. Was, J. Nucl. Mater. **504**, 122 (2018).
https://doi.org/10.1016/j.jnucmat.2018.03.024
51. G. Yeli, V. C. I. Strutt, M. A. Auger, P. A. J. Bagot, and M. P. Moody, J. Nucl. Mater. **543**, 152466 (2021).
https://doi.org/10.1016/j.jnucmat.2020.152466
52. E. A. Kuleshova, B. A. Gurovich, Z. V. Bukina, A. S. Frolov, D. A. Maltsev, E. V. Krikun, D. A. Zhurko, and G. M. Zhuchkov, J. Nucl. Mater. **490**, 247 (2017).
https://doi.org/10.1016/j.jnucmat.2017.04.035
53. Ch. Xu and G. S. Was, J. Nucl. Mater. **454**, 255 (2014).
https://doi.org/10.1016/j.jnucmat.2014.07.062
54. S. V. Rogozhkin, A. A. Nikitin, A. A. Aleev, A. B. Germanov, and A. G. Zaluzhnyi, Inorg. Mater.: Appl. Res. **4**, 112 (2013).
https://doi.org/10.1134/S2075113313020160
55. K. Wang, Ch. M. Parish, K. G. Field, L. Tan, and Yu. Katoh, J. Nucl. Mater. **547**, 152834 (2021).
https://doi.org/10.1016/j.jnucmat.2021.152834
56. K. G. Field, K. C. Littrell, and S. A. Briggs, Scr. Mater. **142**, 41 (2018).
https://doi.org/10.1016/j.scriptamat.2017.08.022
57. S. V. Rogozhkin, A. A. Bogachev, A. A. Nikitin, A. L. Vasiliev, M. Yu. Presnyakov, M. Tomut, and Ch. Trautmann, Nucl. Instrum. Methods Phys. Res., Sect. B **486**, 1 (2021).
https://doi.org/10.1016/j.nimb.2020.10.017

Translated by Sh. Galyaltdinov